Molecular dynamics framework coupled with smoothed particle hydrodynamics for quantum plasma simulations

Thomas Campbell [1], Pontus Svensson [1], Brett Larder [1,2], Daniel Plummer [1], Sam M. Vinko [1,3] and Gianluca Gregori [1,*]

[1] *Department of Physics, Clarendon Laboratory, University of Oxford, Parks Road, Oxford OX1 3PU, United Kingdom*

[2] *Machine Discovery Ltd., John Eccles House, Oxford, OX4 4GP, United Kingdom*

[3] *Central Laser Facility, STFC Rutherford Appleton Laboratory, Didcot OX11 0QX, United Kingdom*

(Received 10 August 2024; accepted 22 April 2025; published 20 June 2025)

We present a scheme for modeling quantum plasmas in the warm dense matter regime via a hybrid smoothed particle hydrodynamic–molecular dynamic treatment, here referred to as "Bohm SPH." This treatment is founded upon Bohm's interpretation of quantum mechanics for partially degenerate fluids, does not apply the Born-Oppenheimer approximation, and is computationally tractable, capable of modeling dynamics over ionic timescales at electronic time resolution. Bohm SPH is also capable of modeling non-Gaussian electron wave functions. We present an overview of our methodology, validation tests of the single particle case including the hydrogen 1s wave function, and comparisons to simulations of a warm dense hydrogen system performed with wave packet molecular dynamics.

DOI: 10.1103/1gwd-z8zq

I. INTRODUCTION

Warm dense matter (WDM) [1] is an exotic state of matter transitional between a solid and a plasma, inheriting properties from both. There has been growing interest in the laser-driven production, diagnosis, theoretical treatment, and simulation of WDM in the preceding decades. This has been driven by the advent of high power laser facilities and associated progress in inertial confinement fusion experiments (ICF) [2], in which the capsule passes through the WDM regime on the route to ignition [3], and interest in astrophysical objects in which WDM naturally occurs such as the Jovian (and similar exoplanet) interior [4,5], dwarf stars, and neutron star crusts [6].

WDM is characterized by simultaneously having strongly coupled ions and quantum degenerate electrons. These characteristics make WDM difficult to treat theoretically, with perturbative techniques unreliable. A range of simulation techniques have been developed including effective ion-ion interaction molecular dynamics (MD) [7,8], MD with classical electrons interacting via effective pairwise quantum statistical potentials (QSP) [9,11–13], wave packet molecular dynamics (WPMD) [14–16], quantum hydrodynamics (QHD) [17,18], density functional theory coupled to MD (DFT-MD) [19,20], time-dependent density functional theory [21,22], and quantum and path integral Monte Carlo approaches [23–25]. All with different levels of approximation and computational cost. DFT-MD in particular is applied widely in the WDM regime to compute ion dynamics. However, it applies the Born-Oppenheimer approximation, with the electrons treated as an instantaneously adjusting background (adiabatically) and their dynamics not captured.

Dynamic electron behavior is essential to estimation of system transport properties such as thermal and electrical conductivity, and in the experimental WDM field, essential to interpreting x-ray Thomson scattering which is often used to diagnose plasma conditions [26–28]. Moreover, explicit electron dynamics may be important to the accuracy of computed ion dynamics in WDM systems, with the first experimental measurements of ion modes in warm dense methane [29] highlighting the need for accurate *ab initio* results to corroborate and inform future experiments. Investigation of ion modes in a warm dense Aluminium system in Ref. [30] via a simple Langevin noise model that mimicked the effect of dynamic electrons, suggested that a proper description of dynamic ion-electron and electron-electron interactions is required to predict the ion dynamics accurately. This was supported by further work [31] demonstrating significant difference between DFT-MD results for ion diffusion in warm dense hydrogen with results from the nonadiabatic electron force field (eFF) variant of WPMD [32,33]. Recently, this conclusion was challenged in Ref. [34], performing a like-for-like comparison of adiabatic and nonadiabatic methodologies via eFF, although uncertainty and limitations remain in the WPMD construction.

WPMD moves beyond the Born-Oppenheimer approximation with equations of motion derived for the electrons via a variational principle [35]. However, WPMD's employment of a single Gaussian as each electron's wave function can be problematic. At low temperatures in particular, a single

*Contact author: gianluca.gregori@physics.ox.ac.uk

Gaussian is too restrictive to produce proper electron screening or resolve the essential atomic physics, or indeed to capture wave-function breakup [36]. With a more complete description of the electron state, time-dependent DFT also treats the electron motion explicitly and avoids such restrictive forms for the electron density, but is computationally costly and limited to small particle numbers and short timescales.

Another recent approach to modeling WDM nonadiabatically has been to leverage Bohm's approach to quantum mechanics [37] (following similar work by de Broglie [38] and Madelung [39]). The reformulation of the single-particle time-dependent Schrödinger equation yields a continuity and momentum evolution equation, with the latter equivalent to that of a classical system but with an additional potential term produced by the kinetic energy operator, the Bohm potential. The extension of this construction to many-body systems is straightforward (as in Sec. 6 of Ref. [37]), but calculation of the exact Bohm potential in this case is as complex as solving the exact many-body Schrödinger equation, hence some level of approximation is required. Work by Larder *et al* [40] applies a thermally averaged, linearized Bohm potential to capture the quantum kinetic energy of the electrons. This approach applies a two stage methodology where the Bohm potential is first calculated as a function of the equilibrium pair-correlation functions, determined with reference to an ion static structure calculation from an alternative scheme, such as DFT-MD. Once determined, the Bohm potential is then applied in an MD code, equivalent in computational cost to a pairwise classical system.

Here we present a variation of the previous approach for the simulation of WDM: Bohm SPH. In a similar vein to Ref. [40], our platform is nonadiabatic and computationally tractable, able to evolve a warm dense matter system at electronic resolution for ionic timescales. Importantly, however, this work moves beyond the two stage methodology and the form of Bohm force is not restricted to thermal equilibrium. This is accomplished by calculating a many-body quantum Bohm pressure on-the-fly with a smoothed particle hydrodynamic (SPH) solver (introduced in the next section) using Gaussian kernels. A further feature of the Bohm SPH construction is access to the continuous spatially resolved electron density. In our methodology we can use multiple SPH particles to model individual electrons. This means that the overall electron shapes are not restricted to the shape of the SPH particles, but can be arbitrarily complex limited only by the number of particles used.

An initial implementation is provided, where further development would entail generalization of the Coulomb interactions to allow for alternative kernels with more compact support, and more efficient root-finders for determining the optimal SPH kernel scale-lengths. Nonetheless, the method outlined below performs well in tests problems and in particular on a warm dense hydrogen system of the kind that motivates this work.

In Sec. II we outline the theory of the Bohm SPH model. In Sec. III we discuss the implementation of Bohm SPH into a molecular dynamics code LAMMPS [41], demonstrate its conservation, and highlight its performance in single-particle test problems and scalability in many-body systems. In Sec. IV we apply the code on a warm dense hydrogen system, and compare the results to those generated via an anisotropic WPMD code, as discussed in Ref. [42]. The data presented in the figures are openly available from the Oxford Research Archive [10].

II. THEORY

We begin by introducing the SPH methodology, then introduce different force contributions, and finally present the overall Lagrangian solved by Bohm SPH.

Smoothed particle hydrodynamics is a meshless scheme for solving fluid equations, applied widely in fields ranging from astrophysics to the computer games industry [43–45]. It obtains approximate numerical solutions of the equations of fluid dynamics by replacing the fluid with a set of particles, whose equations of motion are determined by interpolating from the continuum equations [46]. Smoothed particle hydrodynamics builds upon the definition of the dirac delta function, defined on a domain Ω such that for some continuous function $A(\mathbf{r})$

$$A(\mathbf{r}) = \int_\Omega d\mathbf{r}' A(\mathbf{r}')\delta(\mathbf{r}-\mathbf{r}'). \tag{1}$$

Then by approximating the delta function with a symmetric kernel function W we can write

$$A(\mathbf{r}) \approx \int_\Omega d\mathbf{r}' A(\mathbf{r}') W(\mathbf{r}-\mathbf{r}', h), \tag{2}$$

where h is the scale of the kernel function. W is chosen so that it tends to a delta function in the limit $h \to 0$. In the SPH scheme the fluid is divided into small mass particles with mass m_b, density ρ_b and position $\mathbf{r}_b$, discretizing the integral in Eq. (2) into a summation gives

$$A(\mathbf{r}) = \sum_b m_b \frac{A_b}{\rho_b} W(\mathbf{r}-\mathbf{r}_b, h), \tag{3}$$

where A_b is the value of the function A at position $\mathbf{r}_b$. Gradients of the quantity $A(\mathbf{r})$ can then be calculated similarly,

$$\nabla A(\mathbf{r}) = \sum_b m_b \frac{A_b}{\rho_b} \nabla W(\mathbf{r}-\mathbf{r}_b, h). \tag{4}$$

In Eq. (4) h is a fixed scale length but can be made into a dynamic per-particle variable. The scale length for particle b, h_b, is set according to the local density through the relation

$$h_b = \zeta \left(\frac{m_b}{\rho_b}\right)^{\frac{1}{\mathrm{d}}}, \tag{5}$$

where d is the dimension of the system, and ζ is a constant that must be larger than 1 for stability [47] and is typically set to approximately 1.3 [48]. This enforces that the mass in the kernel volume (set by h_b) is kept constant [44], ensuring good neighbor support for each SPH particle.

Clearly, knowledge of the density, ρ_b, is needed for any of the previous quantities. The density itself, with dynamic kernel lengths, is computed by

$$\rho_a = \sum_b m_b W(\mathbf{r}_a - \mathbf{r}_b, h_a), \tag{6}$$

which is solved alongside Eq. (5) to determine h_a for each particle, the set $\{h_a\}$. While this is typically done using

root-finding procedures such as Newton-Raphson, we have adopted a simple fixed-point iterator which is faster and sufficient to achieve the accuracy we need, as shown later.

In fact, the SPH density, Eq. (6), is simply the discretization of the continuity equation, where normalized kernel functions $\int_V W dV = 1$ ensure a conservation of total mass. The derivative of the density ρ_b with respect to the coordinate $\mathbf{r}_a$ is also an important quantity in SPH, given by

$$\frac{\partial \rho_b}{\partial \mathbf{r}_a} = \frac{1}{\Omega_b} \sum_c m_c \frac{\partial W_{bc}(h_b)}{\partial \mathbf{r}_a}\bigg|_{\{h_b\}} (\delta_{ba} - \delta_{ca}), \tag{7}$$

where $W_{bc}(h_b) = W(\mathbf{r}_b - \mathbf{r}_c, h_b)$. The derivative term inside the summation keeps the scale lengths $\{h_a\}$ constant, and the term Ω_b is given by

$$\Omega_b = 1 - \frac{\partial h_b}{\partial \rho_b} \sum_c m_c \frac{\partial W_{bc}(h_b)}{\partial h_b}, \tag{8}$$

where from Eq. (5)

$$\frac{\partial h_b}{\partial \rho_b} = -\frac{h_b}{\rho_b \mathrm{d}}, \tag{9}$$

with d the number of dimensions.

As demonstrated in Ref. [45], the equations of motion for the SPH particles are easily derivable from a discrete version of the continuum Lagrangian of hydrodynamics. Such an approach yields the standard momentum equation for SPH

$$\frac{d\mathbf{v}_a}{dt} = -\sum_b m_b \left[\frac{P_a}{\Omega_a \rho_a^2} \frac{\partial W_{ab}(h_a)}{\partial \mathbf{r}_a}\bigg|_{\{h_b\}} + \frac{P_b}{\Omega_b \rho_b^2} \frac{\partial W_{ab}(h_b)}{\partial \mathbf{r}_a}\bigg|_{\{h_b\}} \right], \tag{10}$$

where P is the pressure. To close the equation of motion we need to specify P such that the quantum dynamics are captured. This is the main approximation of our model; that is, the assumption that there exists a *quantum* pressure $P \equiv P_B$ able to describe the motion of an ensemble of particles such that quantum properties emerge in a statistical sense. Such pressure P_B is what we refer to as the quantum Bohm pressure. While this is conceptually very different from the conventional thermodynamic pressure, in all that follows, we take that P_B behaves in the same way as ordinary pressure. This can be justified rigorously starting from the Wigner distribution of the quantum statistical ensemble of particles, and, by taking moments of the Wigner-Boltzmann equation, the corresponding hydrodynamic equations can be derived [49,50]. The quantum pressure tensor takes the form

$$P_B(\mathbf{r}) = -\frac{\hbar^2}{4m} n(\mathbf{r}) \nabla \otimes \nabla \ln n(\mathbf{r}), \tag{11}$$

where $\otimes$ is the outer product, and $n(\mathbf{r})$ is the density of the statistical mixture of particles, defined as the zeroth-order moment of the Wigner distribution. As discussed in Refs. [49,51], in the instance that P_B is diagonal (isotropic), the quantum pressure can be related to a scalar potential [37] via

$$\nabla \cdot P_B = n \nabla V_B, \tag{12}$$

where V_B is given by

$$V_B(\mathbf{r}) = -\frac{\hbar^2}{2m} \frac{\nabla^2 \sqrt{n(\mathbf{r})}}{\sqrt{n(\mathbf{r})}}, \tag{13}$$

although in this work we retain nondiagonal terms in P_B so Eq. (12) does not strictly apply.

In the SPH context, the use of a quantum pressure to determine the particle motion via Eq. (10) was introduced in Ref. [52], and applied to a 1D quantum harmonic oscillator, the nonlinear Schrödinger equation in 2D, and the Gross-Pitaevskii-Poisson equation in 3D. In all cases, it was shown that the correct quantum dynamics were recovered. We also note that to make the problem tractable, in Eq. (11) the density of the mixture is replaced by the single-particle density (the usual particle density function). This is exact for a single particle wave function, but for a many-body electron system, using the total electron density leads to a further approximation that we refer to as QHD; see, e.g., Refs. [18,53–55]. As QHD shows that Eq. (11) must be multiplied by a prefactor of order unity to retrieve the correct equation of state [18], in our model here we simply use Eq. (11) with n being the total electron density and the prefactor set to 1.

The pressure tensor P_B is symmetric. We can expand Eq. (11) for the xy value as an example:

$$P_{B_{xy}} = -\frac{\hbar^2}{4m} n\, \partial_x[\partial_y \ln(n)] = -\frac{\hbar^2}{4m} n\, \partial_x\left[\frac{\partial_y n}{n}\right] = \frac{\hbar^2}{4m}\left[\frac{\partial_x n\, \partial_y n}{n} - \partial_{xy} n\right]. \tag{14}$$

This expression is calculated using an SPH discretization. We use the same as in Ref. [52], but with difference terms in both the first and second derivatives of the density, selected following the conservation analysis discussed in Sec. III A. The Bohm pressure for the xy component of the ath SPH particle is

$$P_{B_{a,xy}} = \frac{\hbar^2}{4m} \sum_b \frac{m_b}{\rho_b}\left[\frac{\partial_x n_b\, \partial_y n_b}{n_b} - \partial_{xy} n_b\right] W_{ab}(h_a). \tag{15}$$

The equations of motion are also discretized in the same way as in Ref. [52], namely, for the x component

$$\frac{dv_a^x}{dt} = -\sum_b m_b \left\{ \frac{[P_{B_{a,xx}}, P_{B_{a,xy}}, P_{B_{a,xz}}]}{\rho_a^2 \Omega_a} \cdot \frac{\partial W_{ab}(h_a)}{\partial \mathbf{r}_a}\bigg|_{\{h_b\}} + \frac{[P_{B_{b,xx}}, P_{B_{b,xy}}, P_{B_{b,xz}}]}{\rho_b^2 \Omega_b} \cdot \frac{\partial W_{ab}(h_b)}{\partial \mathbf{r}_a}\bigg|_{\{h_b\}} \right\}. \tag{16}$$

The energy per unit mass associated with the Bohm pressure in Eq. (15), u_{B_a} for the ath particle, is computed according to

$$\frac{du_{B_a}}{dt} = \frac{1}{\Omega_a \rho_a^2} \sum_b m_b [P_{B_a} \cdot (\mathbf{v}_a - \mathbf{v}_b)] \cdot \frac{\partial W_{ab}(h_a)}{\partial \mathbf{r}_a}\bigg|_{\{h_b\}}. \tag{17}$$

This is analogous to the typical SPH expression for the internal energy evolution, as in Ref. [45], but where we now have a pressure tensor P_{B_a} which operates on the velocity difference vector $(\mathbf{v}_a - \mathbf{v}_b)$, rather than a simple scalar pressure. As discussed above, this expression is derived by taking a further moment of Eq. (10). We will show in Sec. III A that

using u_B as the internal quantum energy of the electron system conserves the total energy.

Finally, we mention that an improvement to implementing the QHD-level Bohm pressure tensor would be to compute the Bohm pressure forces on density distributions belonging to each individual electron in the system. This "Many-Fermion" Bohm approach, as discussed in Ref. [56], was investigated but initial tests indicated that its computational cost was prohibitive, hence a QHD Bohm term is the focus of this work.

Having introduced SPH and the Bohm pressure, we can discuss the general construction of the model. Bohm SPH uses the smoothed particle hydrodynamic solver to calculate the quantum force, where the electron density is modelled by Gaussian SPH particles. The density distribution of the SPH particles is taken to be the charge distribution and used to directly calculate the Coulomb potential which couples the electronic component with point ions. This smearing of the electrons prevents asymptotic ion-electron Coulomb attraction, similar to the wave packets in WPMD being the electron charge density, and somewhat similar to the diffractive form of QSP, such as the Kelbg potential [57,58]. Although the resolution of the SPH distribution is controlled numerically by the kernel sizes and not a de Broglie type scale length as in QSP. To resolve better the electron density we run simulations with more SPH particles than electrons $N_S > N_e$. When doing so, the overall mass and charge density of the system is kept consistent, as well as the charge to mass ratio of SPH particles. We apply confining potentials in this case to localise individual electrons and put the velocities of their centers of mass into a target distribution. This avoids unphysical thermal effects caused by the additional degrees of freedom, discussed at greater length in Sec. II D.

A. Coulomb forces

A central step in our hybrid SPH-MD modeling of the electrons comes in the treatment of the Coulomb interaction. We take the kernel used to interpolate the density and Bohm pressure as the real charge density distribution of each particle. We have adopted a Gaussian kernel function for W because of its readily integrable form, and derived the exact SPH Coulomb equations of motion. A more general treatment of the Coulomb interaction would follow the SPH treatment of softened gravity of Ref. [59], without recourse to a specific kernel function. We leave this to future work.

The Gaussian charge density profile is

$$\rho_{e_b}(\mathbf{r}) = n_b(\mathbf{r})q_b = \frac{q_b}{(\pi h_b^2)^{3/2}} \exp\left(-\frac{|\mathbf{r}-\mathbf{r}_b|^2}{h_b^2}\right), \quad (18)$$

with q_b, $\mathbf{r}_b$, and h_b its fractional charge, center of mass, and scale length (width), respectively. The Coulomb potential between an SPH particle and an ion can then be calculated by the analytic integral

$$V_{ib} = \int d\mathbf{r} \frac{Ze}{4\pi\epsilon_0|\mathbf{r}-\mathbf{r}_i|}\rho_{e_b}(\mathbf{r}), \quad (19)$$

where $\mathbf{r}_i$ is the position of the ion, and Z its charge, yielding with $r_{ib} = |\mathbf{r}_i - \mathbf{r}_b|$,

$$V_{ib} = \frac{Zeq_b}{4\pi\epsilon_0 r_{ib}} \mathrm{erf}\left(\frac{r_{ib}}{h_b}\right). \quad (20)$$

The integral in Eq. (19) assumes a simple point ion with $1/r$ Coulomb interaction. This could also be changed to a pseudopotential to include the effect of core electrons, the form of which can be Gaussian-decomposed to enable analytical solutions.

The procedure for the pairwise SPH particle Coulomb potential is similar, integrating across both Gaussian charge clouds

$$V_{ab} = \iint d\mathbf{r}d\mathbf{r}' \frac{\rho_{e_a}(\mathbf{r})\rho_{e_b}(\mathbf{r}')}{4\pi\epsilon_0|\mathbf{r}-\mathbf{r}'|}, \quad (21)$$

yielding for particles a and b

$$V_{ab} = \frac{q_a q_b}{4\pi\epsilon_0 r_{ab}} \mathrm{erf}\left(\frac{r_{ab}}{\sqrt{h_a^2+h_b^2}}\right). \quad (22)$$

When using dynamic kernel widths, these pairwise potentials actually become many-body, via the particle width h_b dependence on the local density in Eq. (5):

$$\frac{\partial V_{ab}}{\partial \mathbf{r}_c} = \left.\frac{\partial V_{ab}}{\partial \mathbf{r}_c}\right|_{\{h\}} + \sum_d \left.\frac{\partial V_{ab}}{\partial h_d}\right|_{\mathbf{r}_c} \frac{\partial h_d}{\partial \mathbf{r}_c}. \quad (23)$$

It is instructive to expand this expression to the exact form implemented within Bohm SPH. Starting with the first term on the right-hand side of Eq. (23), which is nonzero only for $c = a$ or $c = b$, and defining $h_a^2 + h_b^2 = M_{ab}^2$,

$$\left.\frac{\partial V_{ab}}{\partial \mathbf{r}_a}\right|_{\{h\}} = \frac{\xi_{ab}}{r_{ab}}\left[\left(\frac{2}{\sqrt{\pi}M_{ab}}\right)\exp\left(-\frac{r_{ab}^2}{M_{ab}^2}\right) - \frac{1}{r_{ab}}\mathrm{erf}\left(\frac{r_{ab}}{M_{ab}}\right)\right]\hat{\mathbf{r}}_{ab}, \quad (24)$$

where $\xi_{ab} = q_a q_b/4\pi\epsilon_0$ and $\mathbf{r}_{ab} = \mathbf{r}_a - \mathbf{r}_b$. The second term on the right-hand side of Eq. (23) can be expanded via the chain rule as

$$\sum_d \left.\frac{\partial V_{ab}}{\partial h_d}\right|_{\mathbf{r}_c} \frac{\partial h_d}{\partial \mathbf{r}_c} = \sum_d \left.\frac{\partial V_{ab}}{\partial h_d}\right|_{\mathbf{r}_c} \frac{\partial h_d}{\partial \rho_d}\frac{\partial \rho_d}{\partial \mathbf{r}_c}. \quad (25)$$

The derivative of the pairwise Coulomb potential with respect to kernel scale length h_d is

$$\left.\frac{\partial V_{ab}}{\partial h_d}\right|_{\mathbf{r}_c} = -\frac{2\xi_{ad}h_d}{\sqrt{\pi}M_{ad}^3}\exp\left(-\frac{r_{ad}^2}{M_{ad}^2}\right). \quad (26)$$

Then, the remaining terms follow from the SPH treatment of dynamic kernel lengths and the definition of density, as in Eqs. (7) and (9). We can insert these expressions into an equation for the total electronic Coulomb force acting on an SPH particle

$$\mathbf{F}_a^{ee} = -\frac{\partial \mathrm{V}_C^{ee}}{\partial \mathbf{r}_a} = -\frac{\partial}{\partial \mathbf{r}_a}\sum_{b\neq c}\frac{\xi_{bc}}{r_{bc}}\mathrm{erf}\left(\frac{r_{bc}}{M_{bc}}\right), \quad (27)$$

where V_C^{ee} indicates the total Coulomb potential between SPH particles in the system. After some algebra this can be expressed in compressed form as

$$\mathbf{F}_a^{ee} = \Gamma_a - \theta_a \left.\frac{\partial \rho_a}{\partial \mathbf{r}_a}\right|_{\{h\}} - \sum_{b\neq a}\theta_b m_a \left.\frac{\partial W_{ab}(h_b)}{\partial \mathbf{r}_a}\right|_{\{h\}}, \quad (28)$$

where the respective terms are

$$\Gamma_b = \sum_{c\neq b} \frac{\xi_{bc}}{r_{bc}} \left[\frac{1}{r_{bc}} \mathrm{erf}\left(\frac{r_{bc}}{M_{bc}}\right) - \left(\frac{2}{\sqrt{\pi} M_{bc}}\right) \times \exp\left(-\frac{r_{bc}^2}{M_{bc}^2}\right)\right] \hat{\mathbf{r}}_{bc}, \tag{29}$$

$$\theta_b = \sum_{c\neq b} \frac{2h_b^2 \xi_{bc}}{3\rho_b \Omega_b \sqrt{\pi} M_{bc}^3} \exp\left(-\frac{r_{bc}^2}{M_{bc}^2}\right). \tag{30}$$

Note that the pairwise cutoff for computing Γ and θ are different. Γ has the same cutoff as the Coulomb potential, whereas θ must have the same cutoff as that used for the computation of SPH quantities. This is expected given that the θ forces originate from neighboring SPH particle coordinates determining kernel scale lengths through Eqs. (6) and (5).

The full Coulomb force term for an electronic SPH particle interacting with ions, starting from the potential Eq. (20), is almost exactly equivalent, but with M_{bc} being replaced by h_b and one of the SPH charges replaced by the ion charge $Z_i e$. Notably, however, the Coulomb force acting on the ion by the electronic component is only given by the Γ term above, since the ion coordinates do not determine the dynamic SPH scale lengths. The conservative nature of these expressions are demonstrated in Sec. III A.

B. Symmetry effects

When dealing with a many-fermion system indistinguishable particles cannot exist in the same state. The QHD-level Bohm pressure does not enforce this so we must include symmetry effects via an additional potential. Having focused on implementation of the Bohm term in the first iteration of this model rather than highly accurate exchange effects, we include exchange effects in a simple manner by borrowing a spin-averaged symmetry potential from QSP, which we denote V_P for Pauli exclusion. Precisely we employ the temperature dependent equation derived in Ref. [9] and subsequently applied in MD simulations of thermal relaxation such as [11,12]

$$V_P = k_B T \ln(2) \exp\left[-\frac{1}{\ln(2)} \left(\frac{r}{\lambda_{ee}}\right)^2 \right], \tag{31}$$

where $\lambda_{ee} = \hbar (k_B T m_e)^{-1/2}$. The target temperature is used in Eq. (31) rather than the instantaneous temperature. Taking the derivative of the Pauli potential between the ath and bth particle yields the force

$$\mathbf{F}_{P_a} = -\frac{\partial V_{P_{ab}}}{\partial \mathbf{r}_a} = 2k_B T \left(\frac{\mathbf{r}_{ab}}{\lambda_{ee}^2}\right) \exp\left[-\frac{1}{\ln(2)} \left(\frac{r}{\lambda_{ee}}\right)^2 \right]. \tag{32}$$

When using subelectron resolution in the model, with N_{ppe} SPH particles per electron, the interaction is scaled by $1/N_{\mathrm{ppe}}^2$, and interactions between "same-electron" particles are removed. This conserves the total Pauli potential in the system and, if same-electron particles are on top of one another, replicates the pairwise electron interaction ($N_{\mathrm{ppe}} = 1$). This factor naturally appears in the SPH discretization of the Pauli potential, as shown later.

Additionally, the inclusion of the repulsive Minoo potential in the model helps protect against the tensile instability of SPH [45,60,61], which can otherwise result in an unphysical clustering of SPH particles. Indeed, we have not observed the tensile instability in applications of Bohm SPH thus far.

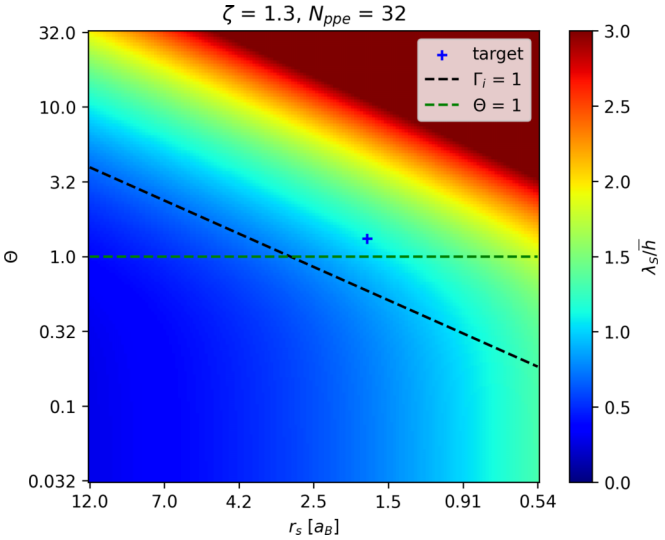

FIG. 1. Ratio of the screening length λ_S to the average SPH kernel width $\bar{h}$ for ionized hydrogen with $N_{\mathrm{ppe}} = 32$. The "target" system is investigated in Sec. IV.

C. SPH resolution

A feature of Bohm SPH is the ability to resolve the electronic component with arbitrary resolution, dependent only on the number of SPH particles used. A useful metric for determining whether the charge density is well resolved is comparison of the average kernel width $\bar{h}$ to the expected screening length of the plasma λ_S, we desire $\bar{h} < \lambda_S$. In the classical and quantum limits the relevant screening lengths will be the Debye λ_D and Thomas Fermi λ_{TF} lengths, respectively. We use equation (6) of Ref. [26] to define the screening length λ_S, which returns λ_D and λ_{TF} in the appropriate limits

$$\lambda_S^{-2} = \kappa_e^2 = \frac{n_e e^2}{\epsilon_0 k_B T_e} \frac{F_{-1/2}(\eta_e)}{F_{1/2}(\eta_e)}, \tag{33}$$

where η_e is the dimensionless chemical potential $\mu_e/k_B T_e$, and F_ν denotes a Fermi integral of order ν.

The requirement of good neighbor support for SPH schemes [47] means that we cannot arbitrarily reduce the kernel widths of the particles. Instead, we increase the number of particles. For the remainder of this manuscript, when discussing systems with N_{ppe} particles per electron, we have scaled all SPH particle masses and charges by $1/N_{\mathrm{ppe}}$ to ensure the correct mass and charge density. Via Eq. (5), we can define the average kernel width $\bar{h}$ for a system with electron density n_e

$$\bar{h} = \zeta (N_{\mathrm{ppe}} n_e)^{-1/3}. \tag{34}$$

Figure 1 demonstrates that we require $N_{\mathrm{ppe}} = 32$ when setting $\zeta = 1.3$ to resolve the warm dense hydrogen system investigated in Sec. IV with Wigner Seitz radius $r_s = (3/4\pi n_e)^{1/3} = 1.75\, \mathrm{a_B}$ and degeneracy parameter $\theta = k_B T/E_F = 1.32$, with $\mathrm{a_B}$ the Bohr radius and E_F the Fermi energy.

D. Confinement potential

We must consider the implication of the ion and electron systems having the same temperature since we are not employing the Born-Oppenheimer approximation. All SPH particles are degrees of freedom and hence contribute to the thermal energy. We generally require $N_S > N_e$ to sufficiently resolve the electron density according to $\overline{h} < \lambda_S$, so the Bohm SPH system will have additional thermal energy compared to the physical one, as demonstrated by equipartition

$$\sum_a^N \frac{1}{2} m_a \langle \mathbf{v}_a^2 \rangle = \frac{3}{2} N k_B T, \tag{35}$$

where T is the target temperature of the system. We assume all $N_S = N_e N_{\text{ppe}}$ SPH particles (with N_e the number of electrons) have identical masses m_s and move at an average speed $\overline{v}$ given by

$$\frac{N_S m_s \overline{v}^2}{2} = \frac{3}{2} N_S k_B T. \tag{36}$$

Since we have N_{ppe} SPH particles per electron, the SPH particle mass scales as $m_s = m_e/N_{\text{ppe}}$ to ensure the correct mass density, so we rewrite Eq. (36) as

$$\frac{m_e \overline{v}^2}{2N_{\text{ppe}}} = \frac{3}{2} k_B T. \tag{37}$$

Rearrangement of Eq. (37) yields

$$\overline{v} = \sqrt{\frac{3N_{\text{ppe}} k_B T}{m_e}}, \tag{38}$$

demonstrating how the average, and indeed the thermal, speed of the SPH particles scales proportionally to $\sqrt{N_{\text{ppe}}}$, causing an unphysical Bohm-Gross dispersion and a spurious ion screening.

This problem is not unique to Bohm SPH. In fact it also appears in particle-in-cell simulations. There, the temperatures of charge macroparticles are typically scaled by the macroparticle weight to address unphysical velocities [62,63]. In our case we cannot apply a general scaling as the ions in our model are not treated identically to the electrons, but as point-particles whose temperature must be fixed at T.

One approach for addressing this problem would be to model the ions and electrons under separate thermostats, with ions at T and electrons at T/N_{ppe}. This can be problematic for collecting reliable ion trajectories as large values of N_{ppe} demand a strong thermostat to prevent the ions equilibriating with the SPH bulk.

An alternative approach, used in this work, is to introduce a quadratic confining potential to localise individual electrons and to apply a thermostat to their centers of mass, which are subsequently released into an NVE (microcanonical) ensemble. After equilibriating these centers of mass at the target temperature, plasmon data computed from their trajectories then avoids the numerical Bohm-Gross dispersion mentioned above. Furthermore, the trajectory data is collected while the whole system is in NVE rather than the ionic and electronic components being maintained at separate temperatures.

SPH particles are allocated a parent electron and forced toward their center of mass via the potential

$$V_C(\mathbf{r}_a) = g|\mathbf{r}_a - \mathbf{R}|^2, \tag{39}$$

where g is varied to adjust the size of the parent electron, $\mathbf{r}_a$ is the position of a target particle, and the center of mass $\mathbf{R} = \sum_b \mathbf{r}_b / N_{\text{ppe}}$ for equal mass particles. In a system with periodic boundary conditions, the center of mass is calculated according to the formulation of Ref. [64]. The confinement force on a particle is given by

$$\mathbf{F}_{\mathbf{C_a}} = -\frac{\partial \sum_b V_{C_b}(\mathbf{r_b})}{\partial \mathbf{r}_a}, \tag{40}$$

where the sum is over the N_{ppe} SPH particles which belong to the same center of mass. This can be expanded as

$$\mathbf{F}_{\mathbf{C_a}} = -\frac{2g}{N_{\text{ppe}}} \left[(\mathbf{r}_a - \mathbf{R})(N_{\text{ppe}} - 1) - \sum_{b \neq a} (\mathbf{r}_b - \mathbf{R}) \right]. \tag{41}$$

In a box without periodic boundary conditions, this simply reduces to

$$\mathbf{F}_{\mathbf{C_a}} = 2g(\mathbf{R} - \mathbf{r}_a), \tag{42}$$

but with periodic boundary conditions, the vectors $\mathbf{r}_a - \mathbf{R}$ need to be computed using the correct (closest) projection of $\mathbf{R}$, which can be the overall center of mass plus or minus a box length in all principal directions $\mathbf{R} \pm L\hat{\mathbf{i}}$. This does not necessarily reduce to Eq. (42).

As stated earlier, we remove the repulsive Coulomb and Pauli potentials between particles belonging to the same electron, while retaining the Bohm interaction. We perform a scan of g values when comparing outputs from Bohm SPH to anisotropic WPMD in Sec. IV.

E. Full Lagrangian

It is instructive to consider the full Lagrangian of the Bohm SPH model. Using the interactions listed above, we can define a Lagrangian for a quantum plasma system with electron density $n(\mathbf{r})$ and N_I point ions. To start, we include self interactions and omit the confining potential

$$\begin{aligned} \mathfrak{L} = &\sum_{i=1}^{N_I} \left[\frac{1}{2} M_i \mathbf{v}_i^2 - \sum_{j>i}^{N_I} \frac{(Ze)^2}{4\pi\epsilon_0 |\mathbf{r}_i - \mathbf{r}_j|} \right] + \int d\mathbf{r}\, n(\mathbf{r}) \\ &\times \left\{ \frac{1}{2} m_e \mathbf{v}(\mathbf{r})^2 - m_e u_B(\mathbf{r}) - \sum_i^{N_i} \frac{Ze^2}{4\pi\epsilon_0 |\mathbf{r}_i - \mathbf{r}|} \right. \\ &\left. - \int d\mathbf{r}' \frac{n(\mathbf{r}')}{2} \left[\frac{e^2}{4\pi\epsilon_0 |\mathbf{r}' - \mathbf{r}|} + V_P(|\mathbf{r}' - \mathbf{r}|) \right] \right\}, \end{aligned} \tag{43}$$

where M_I is the ion mass, Z its ionization, u_B the Bohm energy per unit mass associated with the pressure tensor, and n the number density of electrons, with a factor of $1/2$ included in the second integral to prevent double counting. Now, for the electron kinetic, Bohm, and Pauli terms, we apply the SPH discretization, while for the Coulomb interactions we integrate exactly using the charge density distribution given by the SPH Gaussian kernels. This procedure eliminates all the integral terms, replacing them with summations that can

be implemented into a molecular dynamics structure. Furthermore, we remove the Coulomb and Pauli interactions between SPH particles belonging to the same parent electron and, if enabled, introduce confining potentials for each electron. With N_S SPH particles we have

$$\begin{aligned}\mathfrak{L} = &\sum_{i=1}^{N_I}\left(\frac{1}{2}M_i\mathbf{v}_i^2 - \sum_{j>i}^{N_I}\frac{(Ze)^2}{4\pi\epsilon_0 r_{ij}}\right)\\ &+\sum_{a=1}^{N_S}\left\{\frac{1}{2}m_a\mathbf{v}_a^2 - m_a u_{B_a} - \sum_{i=1}^{N_I}\left[\frac{Zeq_a}{4\pi\epsilon_0 r_{ia}}\mathrm{erf}\left(\frac{r_{ia}}{h_a}\right)\right]\right.\\ &\left.-\sum_{b=1}^{N_S'}\frac{1}{2}\left[\frac{q_a q_b}{4\pi\epsilon_0 r_{ab}}\mathrm{erf}\left(\frac{r_{ab}}{\sqrt{h_a^2+h_b^2}}\right)+\frac{1}{N_{\mathrm{ppe}}^2}V_P(r_{ab})\right]\right\}\\ &-\sum_{c=1}^{N_e}\sum_{d=1}^{N_{\mathrm{ppe}}}[g|\mathbf{r}_d-\mathbf{R}_c|^2]. \end{aligned} \tag{44}$$

Here the SPH variables have subscript a and b, with m_a the SPH particle mass, q_a its fractional charge, $h_a = h_a(\rho_a)$ its dynamic kernel width, and $r_{ab} = |\mathbf{r}_a - \mathbf{r}_b|$. N_S' indicates that particles b belonging to the same electron as particle a are excluded, and where the index c runs over N_e whole electrons and d over N_{ppe} members of each electron.

III. NUMERICS

Bohm SPH has been implemented via modification of LAMMPS, an open-source classical molecular dynamics code with a focus on materials modeling [41]. This includes routines for the Bohm, Pauli, real-space Coulomb interactions (compatible with the Ewald decomposition [65]), a fixed point iterator for computing kernel widths from local densities, confining potentials compatible with periodic boundary conditions [64], as well as a Nosé-Hoover thermostat [66] that operates on the electron centers of mass rather than the SPH particles. Simulations are performed using a velocity-Verlet integrator.

A. Conservation

Following the equations of motion for SPH particles of the previous section, we demonstrate their conservative properties. First, we begin by comparing various forms for the density derivatives used in the Bohm pressure tensor on a simple periodic box interacting only through the Bohm pressure force. We list the mass densities here, but note that number densities are required in the Bohm expressions, simply related by $n = \rho/m_e$ with m_e the electron mass in the appropriate unit. It is well established in the SPH method that naïve derivatives of Eq. (3), as in Eq. (4), are not the most accurate [67–69]; in fact, various alternative expressions exist for SPH derivatives. The forms and associated names investigated here are, for the first derivative,

$$\text{basic:}\ \ \partial_x\rho_a = \sum_b m_b\,\partial_x W_{ab}(h_a), \tag{45}$$

$$\text{F2:}\ \ \partial_x\rho_a = \sum_b m_b\left(1-\frac{\rho_a}{\rho_b}\right)\partial_x W_{ab}(h_a), \tag{46}$$

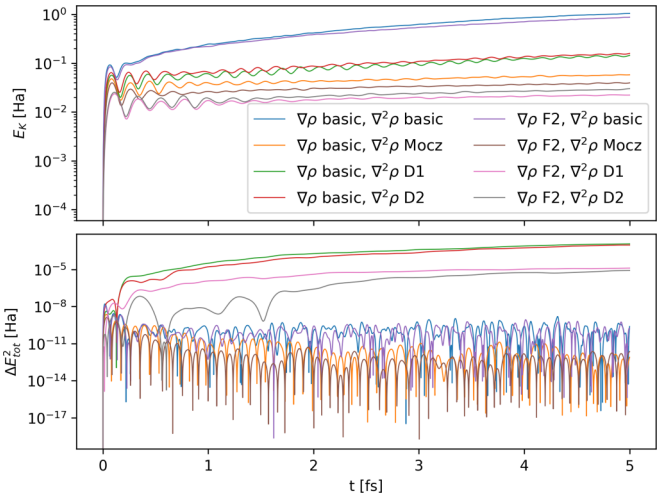

FIG. 2. Kinetic energy and the square of the total energy drift of a Bohm-only system with different derivative combinations.

where "F2" is borrowed as a label from Ref. [67], and for the second derivative

$$\text{basic:}\ \ \partial_{xy}\rho_a = \sum_b m_b\,\partial_{xy}W_{ab}(h_a), \tag{47}$$

$$\text{Mocz:}\ \ \partial_{xy}\rho_a = \sum_b m_b\left(1-\frac{\rho_a}{\rho_b}\right)\partial_{xy}W_{ab}(h_a), \tag{48}$$

$$\text{D1:}\ \ \partial_{xy}\rho_a = \sum_b \frac{m_b}{\rho_b}\,\partial_y\rho_b\,\partial_x W_{ab}(h_a), \tag{49}$$

$$\text{D2:}\ \ \partial_{xy}\rho_a = \sum_b \frac{m_b}{\rho_b}\left(\partial_y\rho_b - \partial_y\rho_a\right)\partial_x W_{ab}(h_a), \tag{50}$$

where "Mocz" corresponds to the form used in Ref. [52]. It is worth noting that the second derivatives D1 and D2 are not symmetric $\partial_{xy} \neq \partial_{yx}$, meaning the Bohm pressure tensor is no longer symmetric. They also require an additional loop over neighbors to compute the first derivative terms.

The eight combinations of derivatives are used on an 1024 SPH particle system, with total mass equivalent to 16 electrons in a cubic box of length 7.11 a_B, the same density as the electrons in the warm dense hydrogen system in the following section. All simulations are initialized identically from rest with timestep 0.1 as, $\zeta = 1.3$ and cutoff $3\,\overline{h}$. The energy outputs are plotted in Fig. 2. All combinations of derivatives conserve momentum to machine precision, as shown in the Appendix. The drift of the total energy ΔE_{tot} is less uniform. The change in total energy for the Bohm-only system is calculated according to

$$\Delta E_{\mathrm{tot}}(t+\delta t) = E_K(t+\delta t) + \Delta U_B - E_K(t), \tag{51}$$

where $E_K =$ is the total kinetic energy of the SPH particles and where the total change in Bohm energy ΔU_B is computed via

$$\Delta U_B = \sum_a m_a \delta t\,\frac{du_{B_a}}{dt}, \tag{52}$$

TABLE I. Energy conservation of derivative combinations for a test Bohm-only simulation with periodic boundary conditions, sorted from best to worst, all to three significant figures.

$\nabla\rho$	$\nabla^2\rho$	$\int \Delta E_{\text{tot}}^2 dt$ [Ha^2 fs]
F2	Mocz	1.01×10^{-11}
Basic	Mocz	2.05×10^{-11}
F2	Basic	9.62×10^{-11}
Basic	Basic	1.29×10^{-10}
F2	D2	1.13×10^{-6}
F2	D1	2.89×10^{-6}
Basic	D2	0.000136
Basic	D1	0.000191

with $\frac{du_{B_a}}{dt}$ calculated according to Eq. (17) using velocity and position data at $t + \delta t$.

A summary of the energy conservation is given in Table I, where ΔE_{tot} is squared and summed over the 5 fs duration of the simulation as an indicator of energy conservation.

The combination of F2 for the first and Mocz for the second derivative seems to be optimal for computing the Bohm pressure tensor in a system with periodic boundary conditions, having the best energy conservation. Derivatives D1 and D2 have surprisingly poor conservation, which we speculate may be related to the breaking of symmetry in the second derivatives.

Next we investigate the conservation of the Coulomb SPH force expressions on a one-component-plasma (OCP) system. The periodic box has 5248 particles, corresponding to 82 electrons, with length 12.261 a_B, once again at the same density of electrons in the warm dense hydrogen system of the following section. All particles interact only via long-range Coulomb potentials. For comparison, both the SPH Coulomb interaction and the standard point Coulomb interaction are examined, with identical initializations of a random particle arrangement. Specifically, the standard LAMMPS interaction coul/long is used for the points. The simulations are run with a timestep of 0.5 as, $\zeta = 1.3$, a real-space cutoff of $r_c = 5.5\,a_B$, and a ewald parameter equal to $3/r_c$. The energy outputs are shown in Fig. 3. In this Coulomb-only system, the total energy E_{tot} is simply the sum of the particle kinetic energies and all the pairwise Coulomb potentials, in the SPH case computed according to Eq. (22). SPH Coulomb conserves momentum to machine precision as shown in the Appendix. After an initial jump, the total energy of the SPH Coulomb system oscillates with similar amplitude to that of the point Coulomb, and the kinetic energy of the SPH Coulomb system equilibrates at a lower value than the point Coulomb as expected. This validates the conservation of the novel SPH Coulomb interaction.

B. Scaling

The bespoke SPH module, utilizing the LAMMPS framework, has excellent parallel scaling. Our module is separate to one previously implemented in LAMMPS (see Ref. [70]). The strong scaling of the warm dense hydrogen system investigated in Sec. IV, at a density of $n_e = 3.006\,\text{g/cm}^3$ and temperature $T = 21.54\,\text{eV}$, with 512 protons and 16 384 SPH electron particles ($N_{\text{ppe}} = 32$), with all interactions computed

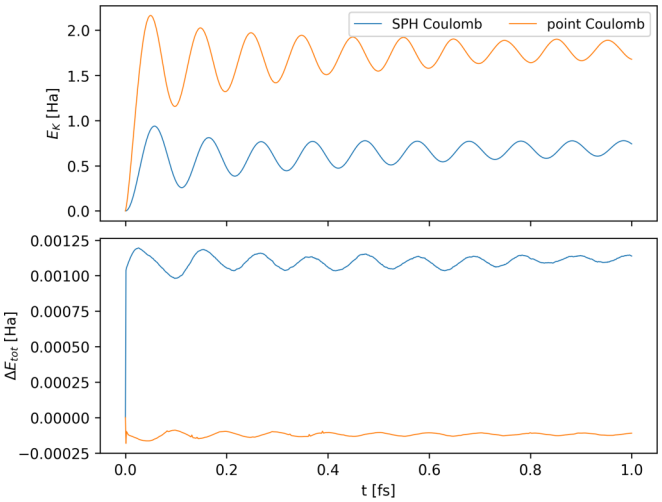

FIG. 3. Kinetic energy and drift of the total energy drift of a test OCP Coulomb-only system comparing standard point and SPH Coulomb interactions.

(Coulomb, Bohm, Pauli, and Confinement) is demonstrated in the left inset of Fig. 4. The scaling contributions from modules within LAMMPS are also plotted alongside the total time. Perfect scaling is given by the relation

$$t_N = t_1/N, \tag{53}$$

where t_N is the wall time per timestep for a simulation running on N processors. We see in Fig. 4 that in the example warm dense hydrogen system, the compute time only begins to notably diverge from perfect scaling at around 100 CPU. This divergence is also dependent on the system size and cutoff radii values for the various force interactions, and hence can be tuned with variation of these parameters.

The weak scaling of Bohm SPH is presented in the right inset of Fig. 4, with consistent compute times observed across the number of processors. The weak scaling is computed with the resolution kept constant and the box size increased. As shown in Fig. 4, the most computationally intensive parts of Bohm SPH are "Pair" and "Modify." The SPH Bohm pressure force and Coulomb forces comprise the majority of the "Pair" compute time, while the calculation of the densities, dynamic kernel scale lengths and centers of mass comprise almost all the "Modify" compute time. Using an alternative kernel with better compact support and therefore smaller neighbor cutoffs, such as the cubic spline [71], would speed up future implementations.

C. Oscillator ground state

In the ground-state tests of the oscillator and hydrogen, we did not use F2 (46) for the first-order density derivatives as we found it caused greater instability than a basic derivative (45) in these particular cases that have a free boundary. SPH schemes generally require special care to handle free boundaries [48]. We have not taken such care due to our systems of interest being continuous plasmas treated with periodic boundary conditions. Despite this, Bohm SPH demonstrates good agreement on two single particle problems which have

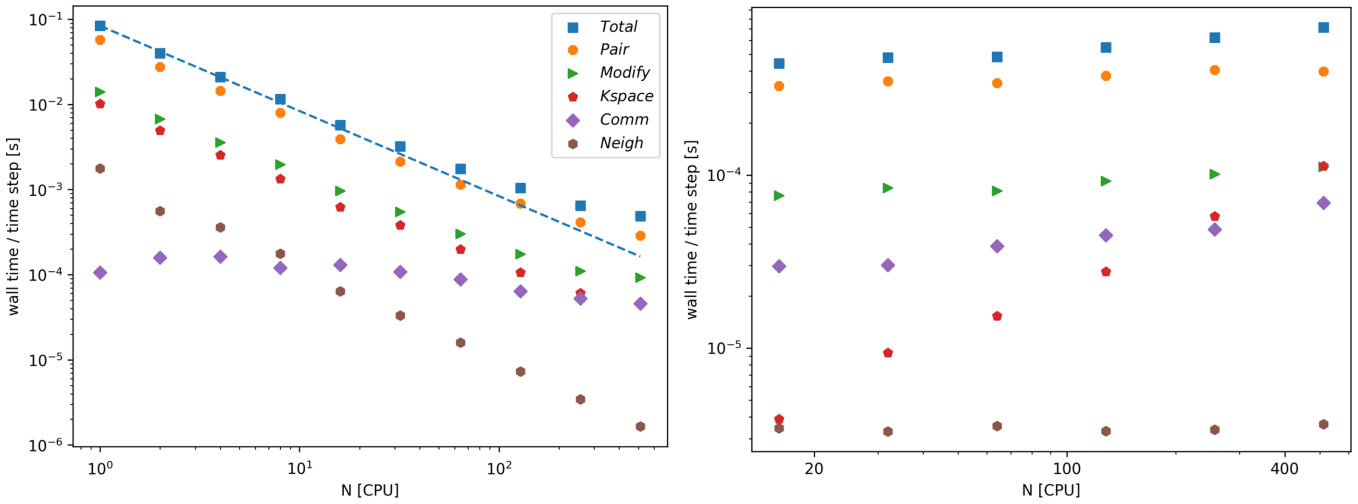

FIG. 4. Strong (left) scaling of a warm dense hydrogen system with 512 protons and 16384 SPH particles, and weak (right) scaling of the same warm dense hydrogen system with a resolution of $N_{\text{ppe}} = 32$ SPH particles per electron. Includes runtime statistics for individual LAMMPS modules. Perfect scaling is indicated by the dashed blue line. The individual module contributions are: the real space force computation in "Pair," the dynamic electron width and center of mass computation within "Modify," Ewald Coulomb calculation in "Kspace," neighbor list construction in "Neigh," and communication times between MPI processors in "Comm."

analytical solutions: the ground states of the 3D quantum harmonic oscillator and the hydrogen atom.

To validate the Bohm expressions used, we first investigate a reduced system interacting only via the Bohm pressure force and a quadratic confining potential. Unlike in many-electron simulations the confining potential here is centered on a fixed coordinate rather than the center of mass of the SPH distribution. Running simulations with $N_S = 256$ SPH particles and dynamic kernel widths we damp the system to zero temperature to achieve the ground state of a quantum harmonic oscillator. In this single wave-function example, the Bohm equations are exact. Taking a Gaussian probability density profile as shown below, equating the expectation energies of the confining potential and the Bohm potential gives a simple relation between the confining potential strength g and the wave-function width H. The Gaussian ground-state density distribution is

$$n(\mathbf{r}) = |\psi(\mathbf{r})|^2 = \frac{1}{(\pi H^2)^{3/2}} \exp\left(-\frac{|\mathbf{r}|^2}{H^2}\right), \tag{54}$$

where H is the overall width of the wave function. Here the confining potential is centered on the origin, and has expectation energy

$$\langle V_c \rangle = \int d\mathbf{r}\, g r^2 |\psi(\mathbf{r})|^2 = \frac{3H^2 g}{2}, \tag{55}$$

and the expectation of the Bohm potential

$$\begin{aligned}\langle V_B \rangle &= \int d\mathbf{r} \left(-\frac{\hbar^2}{2m}\frac{\nabla^2\sqrt{n(\mathbf{r})}}{\sqrt{n(\mathbf{r})}}\right)|\psi(\mathbf{r})|^2 \\ &= \int d\mathbf{r}\, \frac{\hbar^2}{2mH^2}\left(3 - \frac{r^2}{H^2}\right)|\psi(\mathbf{r})|^2 = \frac{3\hbar^2}{4mH^2},\end{aligned} \tag{56}$$

then equating (55) and (56) yields

$$H = \left(\frac{\hbar^2}{2mg}\right)^{1/4}. \tag{57}$$

After damping, the particles are released into an NVE ensemble to check the stability of the solution and the density distributions are fitted to a Gaussian. The fitted Gaussian widths from four simulations sampling different confining strengths g are summarized in Fig. 5, and show excellent agreement with the expected relation (57), validating the implementation of the Bohm pressure tensor.

D. Hydrogen ground state

Now we further test our implementation of the Bohm and the Coulomb forces by attempting to solve for the ground state of hydrogen. For this single electron system, we do

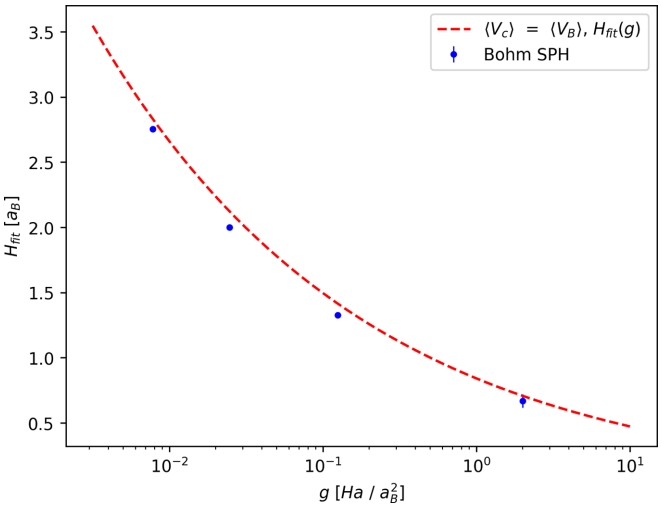

FIG. 5. Fitted Gaussian width outputs from reduced Bohm SPH simulations of a damped quantum harmonic oscillator compared to expected relation [Eq. (57)]. Plotted error is the standard deviation of the width calculations of the final 200 time steps (50 as) of each run, only visible in the strongest confinement point.

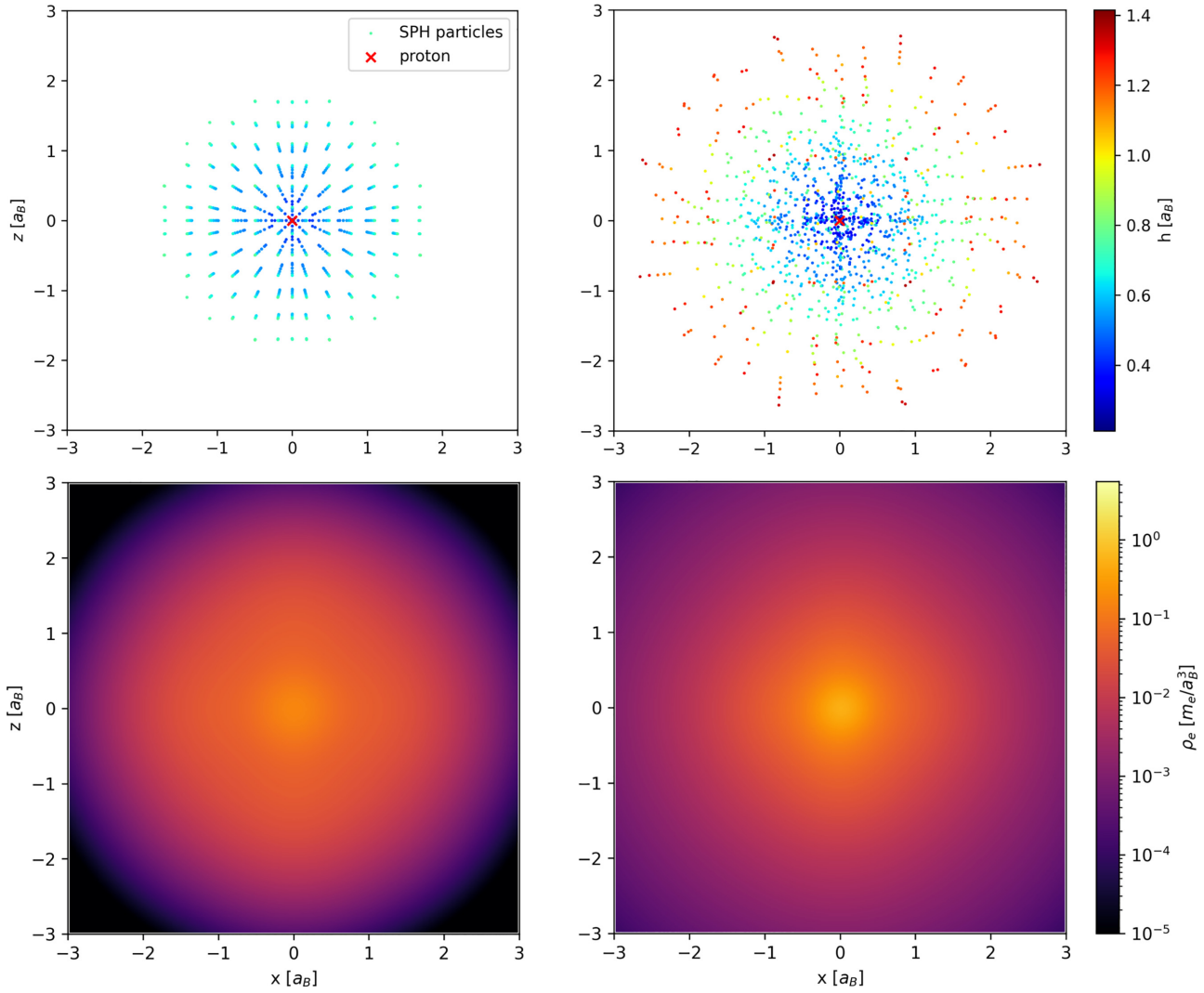

FIG. 6. Initial (left) and final ($t = 1.44$ fs, right) SPH particle distributions for damped Bohm SPH simulation of the hydrogen ground state with particles initialized within a spherical cutoff $r_0 = 2.0\,\mathrm{a_B}$ of the proton. SPH particle position and width (h) information (top) and continuous density profile of cross-section at $y = 0$ (bottom).

not include the Pauli interaction, Coulomb potentials between SPH particles, or the confining potential. While the ground state of the harmonic oscillator is straightforward to solve in Bohm SPH and relatively insensitive to initial distribution and damping strength, the ground state of hydrogen is more challenging. It is difficult to fully suppress the kinetic energy of the SPH particles. We attribute this to the strength of attraction between electron SPH particles and the central ion [Eq. (20)] being not only a function of radial separation, but also of the dynamic kernel widths which are dependent on the many-body distribution.

SPH particles are first initialized on a simple cubic grid around the proton. Comparisons of different starting grids used $N_S = 1237$ SPH particles. The cubic grid terminates within spherical limits to give the system rough initial spherical symmetry. Three initial cutoffs were investigated, $r_0 = 2.0\,\mathrm{a_B}$, $2.5\,\mathrm{a_B}$, and $3.0\,\mathrm{a_B}$, with lattice parameters of $0.3\,\mathrm{a_B}$, $0.375\,\mathrm{a_B}$, and $0.45\,\mathrm{a_B}$, respectively. The particles are randomly displaced off the grid points prior to running by $0.005\,\mathrm{a_B}$ to break the exact symmetry. The simulations are all then run with a time step of 5×10^{-4} as with a frictional damping term applied, of strength $1 \times 10^{-4}\,\mathrm{Ha\,fs/a_B^2}$. A value of $\zeta = 1.3 \times \sqrt{2}$ is used to produce larger kernels and promote stability. The initial and final distribution of SPH particles (projected in two dimensions) is shown in Fig. 6 for initial cutoff radius $r_0 = 2.0\,\mathrm{a_B}$. An additional simulation with $N_S = 2469$ on a grid with lattice parameter of $0.3\,\mathrm{a_B}$ which terminated within a radius of $r = 2.5\,\mathrm{a_B}$ was also run to demonstrate convergence of the density and overall energy toward the exact wave-function solution as N_S is increased.

The evolution of the separate $N_S = 1237$ Bohm SPH runs is shown in Fig. 7, which demonstrates each run converging on similar Bohm and Coulomb energies. The average distribution of SPH particles across all three runs in the final 5 snapshots, from $t = 1.36$ to 1.44 fs at 0.02 fs intervals, is plotted in Fig. 8. The energy averages and errors are given in Table II. For reference, the best fit (energy) of a single Gaussian to the hydrogen 1s density distribution, of width $H = 1.33\,a_B$, is also included in the table. It is instructive to compare the different contributions to the total potential. Neglecting for

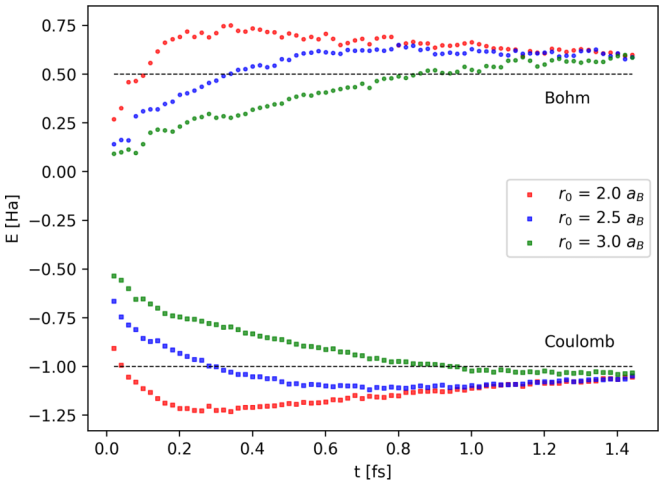

FIG. 7. Energy evolution of damped $N_S = 1237$ Bohm SPH simulations of hydrogen ground state with initial radii r_0=2.0, 2.5, and 3.0 a_B, computed from single snapshots of SPH distribution at 0.02 fs intervals. Squares indicate Coulomb energy, and circles the Bohm energy. Horizontal lines are the exact 1s wave-function energies.

simplicity, nondiagonal entries, the standard Bohm potential calculated for each SPH particle is an expanded form of Eq. (13),

$$V_{B_a} = -\frac{\hbar^2}{8m_e}\left[\frac{2\nabla^2 n_a}{n_a} - \frac{(\nabla n_a)^2}{n_a^2}\right], \tag{58}$$

where the first derivatives of the density are computed without the difference term as in Eq. (45), and the second as

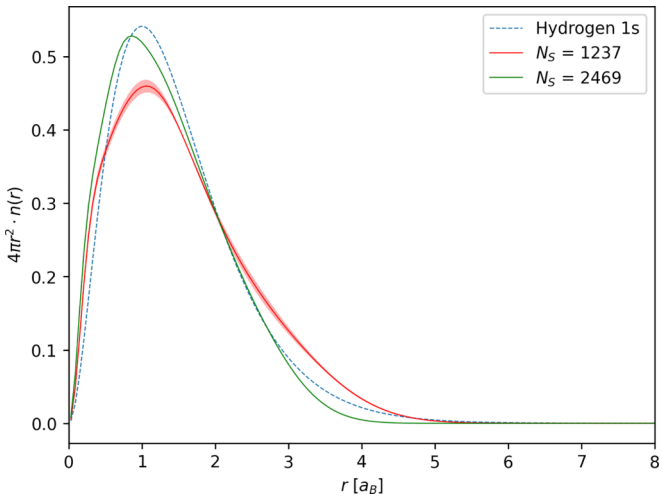

FIG. 8. Density distribution from average of final five snapshots of damped $N_S = 1237$ and $N_S = 2469$ particle Bohm SPH simulations of the hydrogen ground state, compared to exact hydrogen 1s distribution. $N_S = 1237$ average includes values from all three different initial radii, whereas $N_S = 2469$ from a single run with initial radius 2.5 a_B. The average total energy of the $N_S = 1237$ results is $\langle V_{\text{Total}}\rangle = -0.46 \pm 0.01$ Ha, and for $N_S = 2469$ $\langle V_{\text{Total}}\rangle = -0.513 \pm 0.003$ Ha. Central solid line is mean, with error bar $\pm$ the standard deviation.

TABLE II. Comparison of potential energies of the hydrogen ground state computed via damped Bohm SPH simulations with $N_S = 1237$, to the best fit single Gaussian (SG) with width H = 1.33 a_B and to the exact energy contributions of a 1s wave function. Average values of Bohm SPH potentials are calculated from all three runs over five snapshots from $t = 1.36$ to 1.44 fs at 0.02 fs intervals, error given is the standard deviation. All energy values in Hartree units, SG values given to three significant figures.

Type	$\langle V_{\text{Coul}}\rangle$	$\langle V_{\text{Bohm}}\rangle$	$\langle V_{\text{Total}}\rangle$
Bohm SPH	-1.05 ± 0.01	0.59 ± 0.01	-0.46 ± 0.01
SG 1.33 a_B	-0.849	0.424	-0.424
1s	-1.0	0.5	-0.5

in Eq. (48). The total Bohm energy of the system is then $\langle V_{\text{Bohm}}\rangle = \sum_a V_{B_a}/N_S$.

Bohm SPH returns return a total energy value closer to the exact 1s expectation of -0.5 Hartree than the best fit single Gaussian. The convergence of the separate Bohm SPH runs toward a shared ground state, with a more accurate overall energy than the best fit single Gaussian case, validates our treatment of the Coulomb interaction which applies the SPH kernels as real charge distributions.

IV. WARM DENSE HYDROGEN RESULTS

Bohm SPH was used to model a many-body system of spin unpolarized hydrogen at a density of $n_e = 3.006\,\text{g/cm}^3$ and temperature $T = 21.54\,\text{eV}$, corresponding to $\theta = 1.32$ and $r_s = 1.75\,a_B$. At these conditions the ion coupling is $\Gamma_i = (Ze)^2/(4\pi\epsilon_0 a_i k_B T) = 0.72$ with $a_i = r_s$, and the electron plasma period is 0.203 fs. The system has 512 protons and 16384 SPH electron particles ($N_{\text{ppe}} = 32$). Importantly, with the kernel widths dynamically updated according to Eq. (5) with $\zeta = 1.3$, the average SPH kernel width $\bar{h} = 1.16\,a_B$ is less than the expected screening length of the plasma $\lambda_S = 1.29\,a_B$ for these parameters. The system is evolved with a time step of 0.25 as in all simulations.

The following simulations have three stages. A first stage of 50 fs when a thermostat is applied to the ions and the SPH particles remain in NVE to allow them to converge on their centers of mass. A second stage of 250 fs when a thermostat is also applied to the electron centers of mass to bring them to the same temperature as the ions. Finally the third stage of 0.7 ps where both the ions and the SPH particles are released into a microcanonical ensemble in which trajectory data is collected. We note that for our target density and temperature the exact Fermi-Dirac kinetic energy distribution differs only mildly from a Maxwellian, so we have allowed the electrons to relax into a Maxwellian distribution for the collection of trajectory data.

An example of the thermalization of the system is shown in Fig. 9, with the ion temperature T_i and the electron temperature T_e plotted. For free SPH particles the electronic temperature is simply given by Eq. (35). Instead, we are using confining potentials and also a thermostat that operates on the center of mass velocity of each electron $\mathbf{V}_i = \sum_j^{N_{\text{ppe}}} \mathbf{v}_j/N_{\text{ppe}}$. The trajectories of the electron centers of mass are then collected to compute the electronic structure. Hence the center of

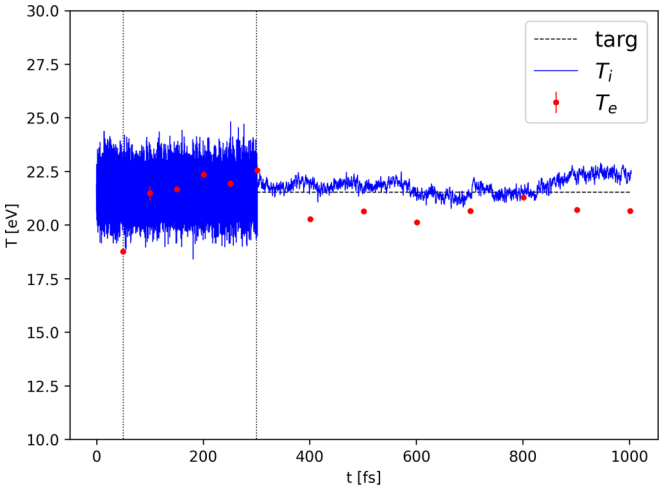

FIG. 9. Temperature data for run of strongest confinement ($g = 8.16\,\mathrm{Ha}/\mathrm{a_B^2}$) of Bohm SPH. "targ" corresponds to the target temperature, T_i the ion temperature, and T_e the electron temperature as defined by Eq. (59). Error bars on T_e are the standard deviation of the temperature computed at 25 individual timesteps separated by 1.0 as each (centre point is mean). The simulation stage boundaries are indicated by the vertical dotted lines.

mass temperature is the electronic temperature of interest to us

$$\sum_i^{N_e} \frac{1}{2} m_e \langle \mathbf{V}_i^2 \rangle = \frac{3}{2} N_e k_B T_e. \tag{59}$$

We scan values of g producing electron sizes between roughly 3.0 and 2.0 $\mathrm{a_B}$ (as shown in Fig. 10), calculated by fitting a single Gaussian to the density distribution of SPH particles belonging to the same electron. At each confinement strength we perform two runs with different initial conditions to average the results. The drift in total energy over the 0.7 ps of data collection when under the strongest confinement is less than 5% of the total kinetic energy at release into NVE. An

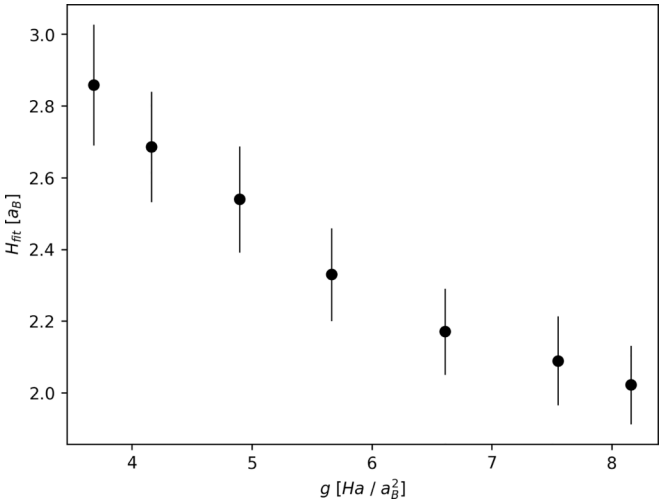

FIG. 10. Mean electron Gaussian widths (± standard deviation) from end of Bohm SPH runs of hydrogen at $\theta = 1.32$ and $r_s = 1.75\,\mathrm{a_B}$ with different confinement strengths g.

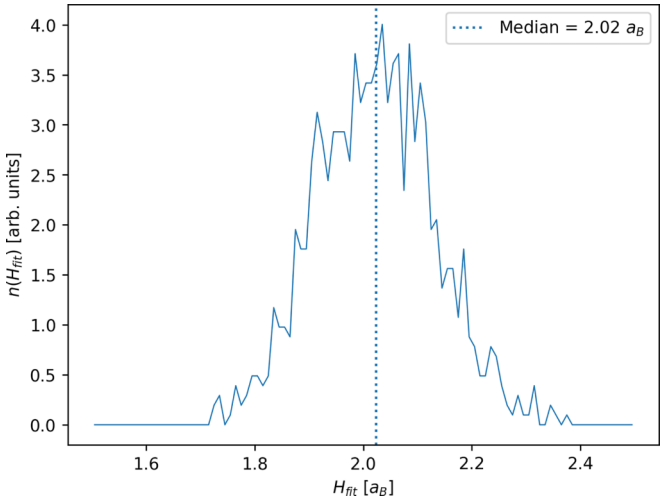

FIG. 11. Fitted electron width distribution from end of Bohm SPH runs with strongest confinement and best agreement to WPMD.

example distribution of the fitted electron sizes in the strongest confinement case is given in Fig. 11. The plateauing trend of mean fitted widths in Fig. 10 suggests substantial further contraction of the electron width may not be feasible with our selected SPH parameters. A larger value of N_{ppe} may allow investigation of smaller electron widths by decreasing the average particle kernel width.

The results are benchmarked against outputs from anisotropic WPMD, in which the root mean square width of the Gaussian wavepackets was $H_W = 1.44\,\mathrm{a_B}$. A key quantity of interest is the dynamic structure factor (DSF), defined for systems in thermodynamic equilibrium as

$$S(\mathbf{k}, \omega) = \frac{1}{2\pi N} \int dt\ \exp(i\omega t) \langle \rho(\mathbf{k}, t) \rho(-\mathbf{k}, 0) \rangle, \tag{60}$$

where N is the number of particles and $\rho(\mathbf{k}, t)$ is the spatial Fourier transform of the time-dependent density $n(\mathbf{r}, t)$. The dynamic structure factor is the power spectrum of the intermediate scattering function [72]

$$F(\mathbf{k}, t) = \frac{1}{N} \langle \rho(\mathbf{k}, t) \rho(-\mathbf{k}, 0) \rangle. \tag{61}$$

The dynamic structure factor describes density fluctuations at wavenumber $\mathbf{k}$ and frequency ω, and is an essential link between theory and experiment, with x-ray thomson scattering deployed to diagnose the density and temperature of dense plasmas in the laboratory [27,28], where the experimentally measured x-ray scattering cross-section is directly proportional to the total dynamic structure factor of the electrons [26,73]. We also examine the static structure factor, calculated via frequency integration of the DSF $S(\mathbf{k}) = \int d\omega\, S(\mathbf{k}, \omega)$, and also related (via Fourier transform) to the pair correlation function. In the following results we assume isotropic and spatially uniform systems such that the structure factors depend only on the magnitude of the wavenumber $k = |\mathbf{k}|$.

When presenting dynamic structure data from Bohm SPH, we have employed the generalized collective modes (GCM) approach, as described in Ref. [74] and deployed in analysis of ionic modes in Ref. [75]. We perform the fits of the intermediate scattering functions using one propagating and

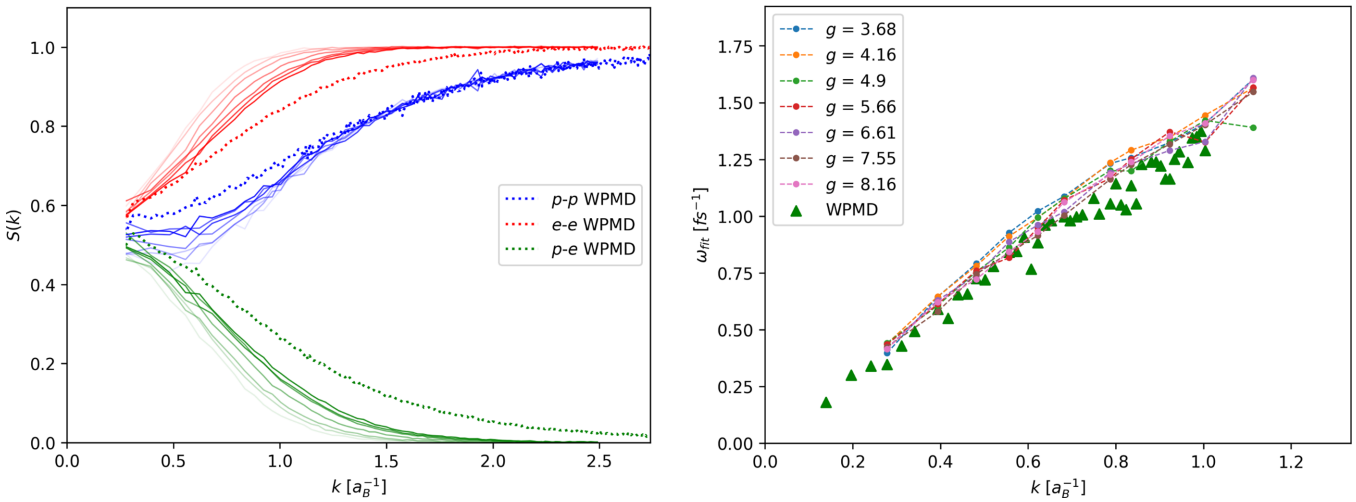

FIG. 12. Left: Proton-proton and electron-electron static structure factors from Bohm SPH runs with confinement compared to reference calculation from WPMD. Values of g as in Fig. 10 with smallest confinement in lightest shade to strongest confinement in darkest, units $\mathrm{Ha/a_B^2}$. Right: Ion dispersion from Bohm SPH scan of confinement strengths. Frequency plotted is the fitted generalized collective modes (GCM) value for the propagating mode.

one diffusive mode, then used to calculate associated dynamic structure factors $S(k, \omega)$.

Figure 12(a) demonstrates that the Bohm SPH static structure calculations have improved agreement with the WPMD calculation as the strength of confinement is increased. Unsurprisingly, the ion-electron and electron-electron structure factors are more sensitive to the strength of confinement. Even in the case of the weakest confinement, however, the ion structure agrees reasonably well with WPMD, and the extrapolated electron and ion structure values at $S(k = 0)$, related to the compressibility [76,77], are similar to the WPMD estimates. We ascribe the difference in static structure observed between Bohm SPH and WPMD to be primarily due to different electron sizes, which strongly affect the screening of the plasma. The strongest confinement case of Bohm SPH achieves an average electron width of $H_{\mathrm{fit}} = 2.02\,\mathrm{a_B}$, still larger than the root mean squared width of the WPMD output of $H_W = 1.44\,\mathrm{a_B}$.

The ion dispersion is relatively insensitive to the confinement strength, as shown in Fig. 12(b). If we also examine the ion dynamic structure factor, as in Fig. 13, we can see relatively good agreement between Bohm SPH and WPMD, with some differences in the strength of the diffusive mode.

Using the center of mass coordinates of each electron recorded over the simulation, and treating them as point particles, we also compute the electron dynamic structure. A commonly used decomposition of the electron dynamic structure factor is given by Chihara [78,79]

$$S_{ee}(\mathbf{k}, \omega) = |f(\mathbf{k}) + n(\mathbf{k})|^2 S_{ii}(\mathbf{k}, \omega) + S^0_{ee}(\mathbf{k}, \omega) + S_{bf}(\mathbf{k}, \omega), \tag{62}$$

where $f(\mathbf{k})$ is the unscreened bound electron form factor, $n(\mathbf{k})$ the screening cloud form factor, $S_{ii}(\mathbf{k}, \omega)$ the ion-ion structure factor, $S^0_{ee}(\mathbf{k}, \omega)$ the free electron structure factor, and $S_{bf}(\mathbf{k}, \omega)$ a scattering contribution from bound-free transitions. In our simulation of ionized hydrogen, with no contribution from $f(\mathbf{k})$ or $S_{bf}(\mathbf{k}, \omega)$ we have access to both $S_{ii}(\mathbf{k}, \omega)$ and $S_{ee}(\mathbf{k}, \omega)$. Comparison of the intermediate scattering functions $F_{ee}(\mathbf{k}, t)$ and $F_{ii}(\mathbf{k}, t)$ enables calculation of the screening cloud form factor $n(\mathbf{k})$ and by extension, isolation of the free electron structure factor $S^0_{ee}(\mathbf{k}, \omega)$ [80]. The screening cloud $n(\mathbf{k})$ can also be computed by comparing the proton-proton and proton-electron static structure factors [78] via $S_{pe}(\mathbf{k}) = n(\mathbf{k}) S_{pp}(\mathbf{k})$ in the case of hydrogen. Here, we compute $n(k)$ (isotropic) by minimizing the loss

$$L = \int dt\, [F_{ee}(k, t) - (n(k))^2 F_{ii}(k, t)]^2. \tag{63}$$

For small values of k in the collective regime $\alpha = 1/k\lambda_S > 1$, we apply the GCM fitting procedure as before with one propagating and one relaxing mode. In addition, we apply a detailed balance correction, as in Ref. [73], of the form $\beta\hbar\omega/(1 - e^{-\beta\hbar\omega})$.

The outputs are plotted in Fig. 14, and they compare favourably with outputs from WPMD, computed via direct fourier transform of the truncated intermediate scattering function and which apply the same detailed balance correction. In the electron dynamic structure factors the effect of confinement is more prominent. Both the position of the plasmon peak and the value of $S^0_{ee}(k, \omega = 0)$ agree more closely with WPMD in the strongly confined case than weakly. The weakly confined case consistently underpredicts the plasmon frequency and overestimates $S^0_{ee}(k, \omega = 0)$, associated with the electron diffusivity, when comparing to WPMD. Figure 15 shows how the plasmon frequency and its width trend with increasing confinement strength. In the collective $\alpha > 1$ regime, the values reasonably converge by the strongest confinement case. With a more pronounced dependence on confinement strength at shorter length scales (smaller α), we see how the achieved electron size determines the resolvable electron dynamics.

The electron dynamic structure outputs are also compared to the predictions of the random phase approximation [77,81], which applies when the interparticle interactions are weak. We note that the numerical outputs for the plasmon (strong confinement Bohm SPH and WPMD) at the investigated k modes predict a lower peak frequency and a slightly broader

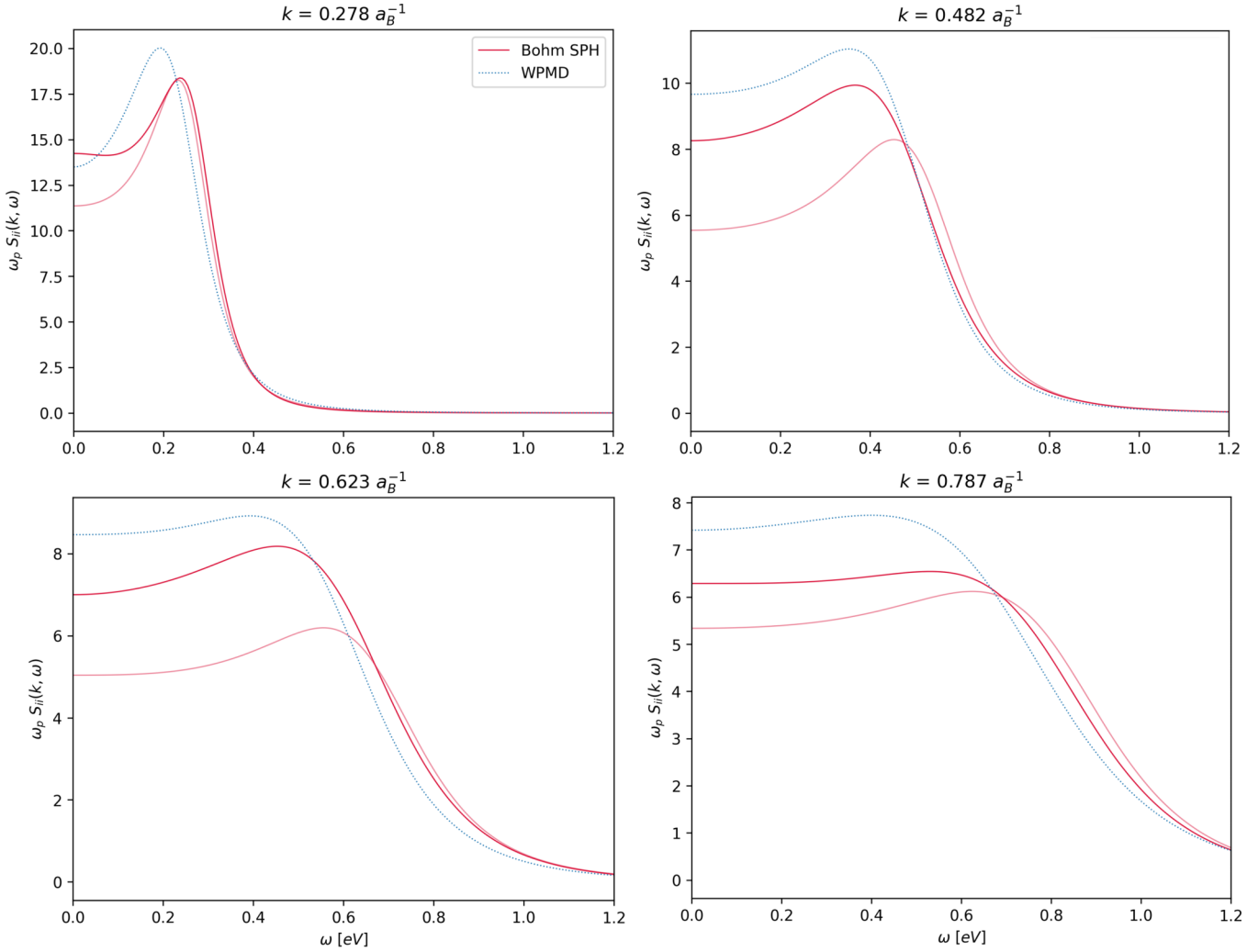

FIG. 13. Ion dynamic structure factors for selected k modes for strongest ($g = 8.16\,\mathrm{Ha/a_B^2}$, dark red) and weakest ($g = 3.68\,\mathrm{Ha/a_B^2}$, light red) confinement. Compared to WPMD outputs (dotted blue).

plasmon. A similar effect has been reported in previous work investigating the impact of exchange-correlation as well as ion collisions on plasmon dispersion [82,83].

V. CONCLUSIONS AND FUTURE WORK

We have presented a new scheme for the simulation of WDM. Advantages of the methodology are its nonadiabatic treatment of ion-electron interactions with explicit electron dynamics, a many-body calculation of the quantum Bohm pressure, the ability to model arbitrary electron shapes, tunable resolution, and computational scalability. After conservations tests, the Bohm and Coulomb implementations of the code were validated by single particle tests of the quantum harmonic oscillator ground state and the hydrogen 1s wave function.

The nonadiabatic treatment of the ion-electron interaction when using more SPH particles than electrons present in the system motivates use of a confining potential to localise individual electrons, whose center of mass velocity can be operated upon by a thermostat to achieve an appropriate distribution.

Bohm SPH was used to simulate a warm dense hydrogen system at $\theta = 1.32$ and $r_s = 1.75\,\mathrm{a_B}$ and compared to outputs from anisotropic WPMD, scanning a range of confinement strengths. In particular, the electron dynamic structure factors of the strongest confinement case agreed well with outputs from WPMD in the collective regime. Comparison of static structure outputs were also encouraging while indicating that a smaller electron size in Bohm SPH would improve agreement with WPMD. More broadly, comparisons of Bohm SPH outputs for the static and dynamic structure factors when scanning the confinement strength show how the electron size affects screening within the plasma.

Several aspects of the methodology might be improved or generalized in future versions. The treatment here is based upon Gaussian kernels, but generalizing the Coulomb interaction to any kernel function would allow use of kernels with better compact support, reducing computational cost. Additionally, the Coulomb interaction could be extended to include the interaction between SPH particles and ions with core electrons via a pseudopotential. Although the fixed-point iterator used in this work to self consistently calculate SPH densities and scale lengths performed well, the Newton-Raphson root

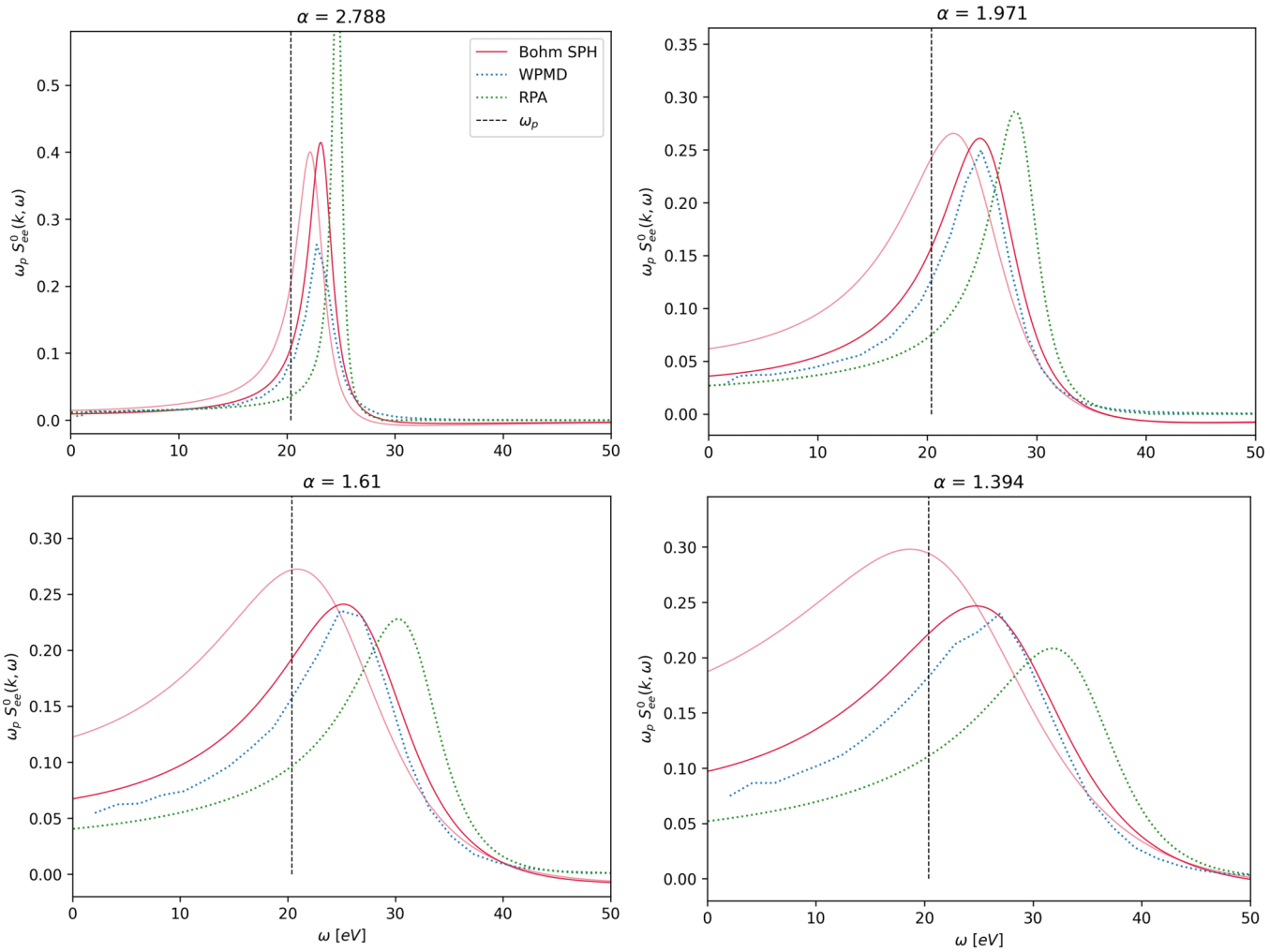

FIG. 14. Free electron dynamic structure factors for collective scattering k values $\alpha > 1/(k\lambda_S)$ for strongest ($g = 8.16\,\mathrm{Ha/a_B^2}$, dark red) and weakest ($g = 3.68\,\mathrm{Ha/a_B^2}$, light red) confinement. Compared to WPMD (dotted blue) and RPA (dotted green) outputs.

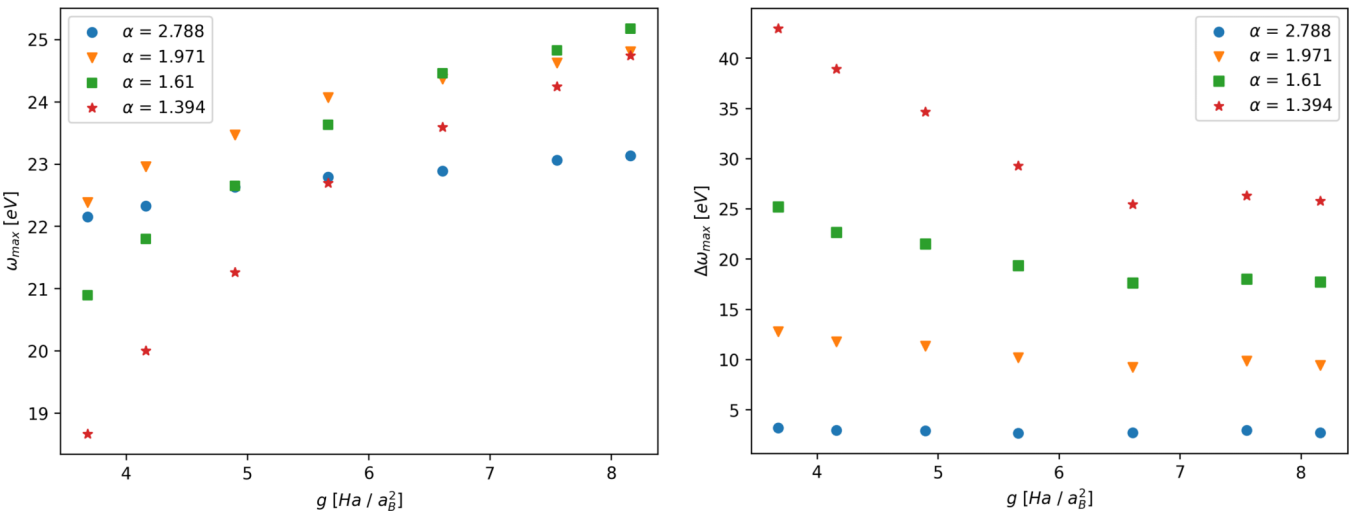

FIG. 15. Maximum value (left) and FWHM of plasmon (right). Computed for collective scattering k values $\alpha > 1/(k\lambda_S)$ across all confinement strengths g sampled.

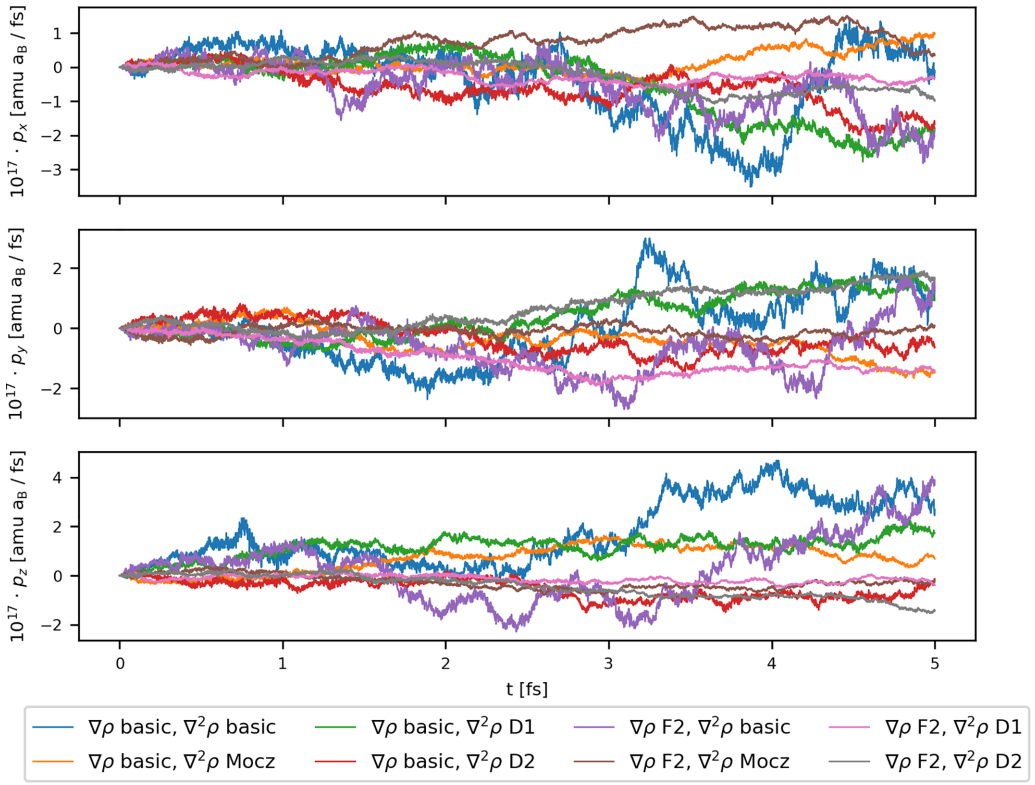

FIG. 16. Total momentum components of a Bohm-only system with different derivative combinations. *Y* axes multiplied by a factor of 10^{17}.

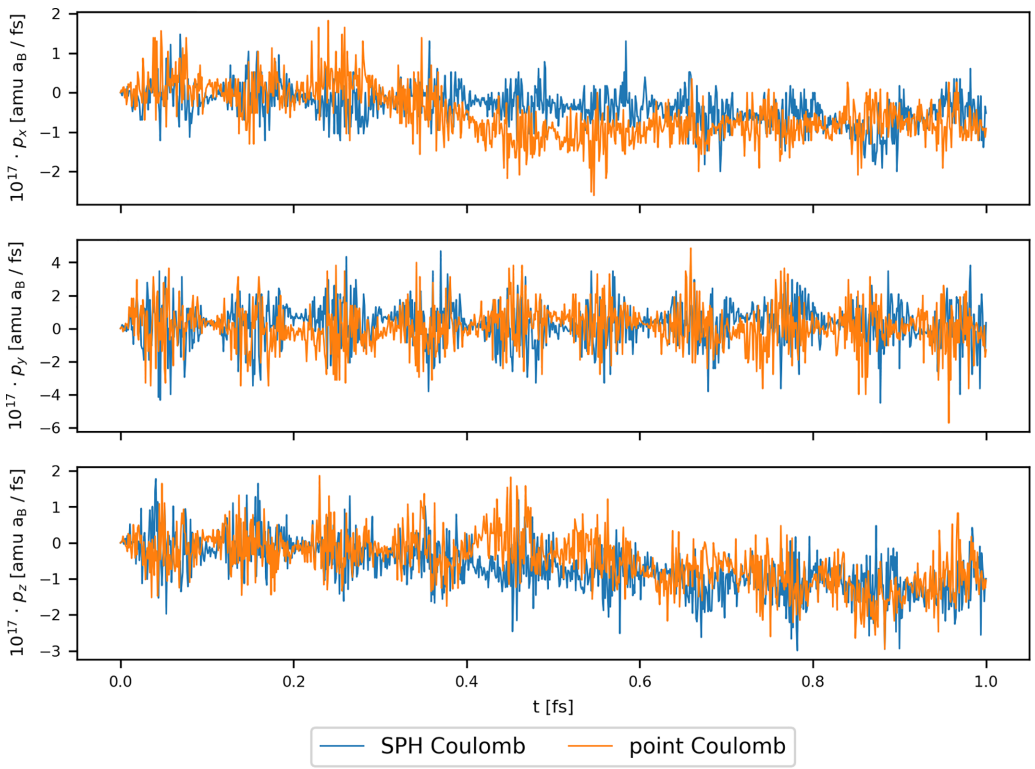

FIG. 17. Total momentum components of a test OCP Coulomb system comparing standard point and SPH Coulomb interactions. *Y* axes multiplied by a factor of 10^{17}.

finding procedure would be preferable. Finally, further forms of density derivative used in computing the Bohm pressure tensor, as compared in Sec. III A, could be explored.

ACKNOWLEDGMENTS

Computing resources were provided by STFC Scientific Computing Department's SCARF cluster. We are grateful to the anonymous referee whose comments improved this paper. T.C. acknowledges useful discussions with Thomas Gawne, Sam Azadi, and Thomas White prior to and during the production of Bohm SPH. T.C. and S.M.V. acknowledge support from the Royal Society and from the UK EPSRC Grant No. EP/W010097/1. P.S. acknowledges funding from the Oxford Physics Endowment for Graduates (OXPEG). P.S., D.P., S.M.V., and G.G. acknowledge support from AWE-NST via the Oxford Centre for High Energy Density Science (OxCHEDS).

DATA AVAILABILITY

The data presented in the figures are openly available [10].

APPENDIX: MOMENTUM CONSERVATION

The momentum conservation data for the test Bohm-only and Coulomb-only systems, displayed in Figs. 16 and 17 respectively, as described in Sec. III A.

[1] D. Riley, *Warm Dense Matter: Laboratory Generation and Diagnosis* (IOP Publishing, Bristol, UK, 2021).
[2] H. Abu-Shawareb, R. Acree, P. Adams, J. Adams, B. Addis, R. Aden, P. Adrian, B. Afeyan, M. Aggleton, L. Aghaian *et al.*, Achievement of target gain larger than unity in an inertial fusion experiment, Phys. Rev. Lett. **132**, 065102 (2024).
[3] S. Hu, L. Collins, T. Boehly, Y. Ding, P. Radha, V. Goncharov, V. Karasiev, G. Collins, S. Regan, and E. Campbell, A review on *ab initio* studies of static, transport, and optical properties of polystyrene under extreme conditions for inertial confinement fusion applications, Phys. Plasmas **25**, 056306 (2018).
[4] T. Guillot, Interiors of giant planets inside and outside the solar system, Science **286**, 72 (1999).
[5] G. I. Kerley, Equation of state and phase diagram of dense hydrogen, Phys. Earth Planet. Inter. **6**, 78 (1972).
[6] J. Daligault and S. Gupta, Electron–ion scattering in dense multi-component plasmas: Application to the outer crust of an accreting neutron star, Astrophys. J. **703**, 994 (2009).
[7] J. P. Mithen, J. Daligault, and G. Gregori, Extent of validity of the hydrodynamic description of ions in dense plasmas, Phys. Rev. E **83**, 015401 (2011).
[8] H. Kählert, Thermodynamic and transport coefficients from the dynamic structure factor of Yukawa liquids, Phys. Rev. Res. **2**, 033287 (2020).
[9] H. Minoo, M. Gombert, and C. Deutsch, Temperature-dependent Coulomb interactions in hydrogenic systems, Phys. Rev. A **23**, 924 (1981).
[10] T. Campbell, *Oxford Research Archive* (2025), https://ora.ox.ac.uk/objects/uuid:20c55326-b389-4aa7-af60-ded75d707795.
[11] J. Hansen and I. McDonald, Thermal relaxation in a strongly coupled two-temperature plasma, Phys. Lett. A **97**, 42 (1983).
[12] J. Glosli, F. Graziani, R. More, M. Murillo, F. Streitz, M. Surh, L. Benedict, S. Hau-Riege, A. Langdon, and R. London, Molecular dynamics simulations of temperature equilibration in dense hydrogen, Phys. Rev. E **78**, 025401 (2008).
[13] G. Dimonte and J. Daligault, Molecular-dynamics simulations of electron-ion temperature relaxation in a classical Coulomb plasma, Phys. Rev. Lett. **101**, 135001 (2008).
[14] E. J. Heller, Time-dependent approach to semiclassical dynamics, J. Chem. Phys. **62**, 1544 (1975).
[15] H. Feldmeier, Fermionic molecular dynamics, Nucl. Phys. A **515**, 147 (1990).
[16] M. Knaup, P. Reinhard, C. Toepffer, and G. Zwicknagel, Wave packet molecular dynamics simulations of warm dense hydrogen, J. Phys. A: Math. Gen. **36**, 6165 (2003).
[17] D. Michta, F. Graziani, and M. Bonitz, Quantum hydrodynamics for plasmas–A Thomas-Fermi theory perspective, Contrib. Plasma Phys. **55**, 437 (2015).
[18] Z. A. Moldabekov, M. Bonitz, and T. Ramazanov, Theoretical foundations of quantum hydrodynamics for plasmas, Phys. Plasmas **25**, 031903 (2018).
[19] T. White, S. Richardson, B. Crowley, L. Pattison, J. Harris, and G. Gregori, Orbital-free density-functional theory simulations of the dynamic structure factor of warm dense aluminum, Phys. Rev. Lett. **111**, 175002 (2013).
[20] H. R. Rüter and R. Redmer, *Ab initio* simulations for the ion-ion structure factor of warm dense aluminum, Phys. Rev. Lett. **112**, 145007 (2014).
[21] C. A. Ullrich, *Time-Dependent Density-Functional Theory: Concepts and Applications* (Oxford University Press, Oxford, UK, 2011).
[22] A. D. Baczewski, L. Shulenburger, M. Desjarlais, S. Hansen, and R. Magyar, X-ray thomson scattering in warm dense matter without the Chihara decomposition, Phys. Rev. Lett. **116**, 115004 (2016).
[23] S. Hu, B. Militzer, V. Goncharov, S. Skupsky *et al.*, First-principles equation-of-state table of deuterium for inertial confinement fusion applications, Phys. Rev. B **84**, 224109 (2011).
[24] B. Militzer, F. González-Cataldo, S. Zhang, K. P. Driver, and F. Soubiran, First-principles equation of state database for warm dense matter computation, Phys. Rev. E **103**, 013203 (2021).
[25] M. Bonitz, T. Dornheim, Z. A. Moldabekov, S. Zhang, P. Hamann, H. Kählert, A. Filinov, K. Ramakrishna, and J. Vorberger, *Ab initio* simulation of warm dense matter, Phys. Plasmas **27**, 042710 (2020).
[26] S. H. Glenzer and R. Redmer, X-ray thomson scattering in high energy density plasmas, Rev. Mod. Phys. **81**, 1625 (2009).
[27] L. Fletcher, A. Kritcher, A. Pak, T. Ma, T. Döppner, C. Fortmann, L. Divol, O. Jones, O. Landen, H. Scott *et al.*, Observations of continuum depression in warm dense matter with x-ray thomson scattering, Phys. Rev. Lett. **112**, 145004 (2014).
[28] H. Poole, D. Cao, R. Epstein, I. Golovkin, T. Walton, S. Hu, M. Kasim, S. Vinko, J. Rygg, V. Goncharov *et al.*, A case

study of using x-ray thomson scattering to diagnose the in-flight plasma conditions of DT cryogenic implosions, Phys. Plasmas **29**, 072703 (2022).
[29] T. G. White, H. Poole, E. E. McBride, M. Oliver, A. Descamps, L. B. Fletcher, W. A. Angermeier, C. H. Allen, K. Appel, F. P. Condamine *et al.*, Speed of sound in methane under conditions of planetary interiors, Phys. Rev. Res. **6**, L022029 (2024).
[30] P. Mabey, S. Richardson, T. White, L. Fletcher, S. Glenzer, N. Hartley, J. Vorberger, D. O. Gericke, and G. Gregori, A strong diffusive ion mode in dense ionized matter predicted by Langevin dynamics, Nat. Commun. **8**, 14125 (2017).
[31] Y. Yao, Q. Zeng, K. Chen, D. Kang, Y. Hou, Q. Ma, and J. Dai, Reduced ionic diffusion by the dynamic electron–ion collisions in warm dense hydrogen, Phys. Plasmas **28**, 012704 (2021).
[32] J. T. Su and W. A. Goddard, The dynamics of highly excited electronic systems: Applications of the electron force field, J. Chem. Phys. **131**, 244501 (2009).
[33] W. A. Angermeier and T. G. White, An investigation into the approximations used in wave packet molecular dynamics for the study of warm dense matter, Plasma **4**, 294 (2021).
[34] W. A. Angermeier, B. S. Scheiner, N. R. Shaffer, and T. G. White, Disentangling the effects of non-adiabatic interactions upon ion self-diffusion within warm dense hydrogen, Phil. Trans. R. Soc. A. **381**, 20230034 (2023).
[35] P. E. Grabowski, A review of wave packet molecular dynamics, Front. Chall. Warm Dense Matter **96**, 265 (2014).
[36] P. E. Grabowski, A. Markmann, I. V. Morozov, I. A. Valuev, C. A. Fichtl, D. F. Richards, V. S. Batista, F. R. Graziani, and M. S. Murillo, Wave packet spreading and localization in electron-nuclear scattering, Phys. Rev. E **87**, 063104 (2013).
[37] D. Bohm, A suggested interpretation of the quantum theory in terms of "hidden" variables. I, Phys. Rev. **85**, 166 (1952).
[38] L. De Broglie, *An Introduction to the Study of Wave Mechanics* (E.P. Button and Company, Inc., New York, 1930).
[39] E. Madelung, Quantum theory in hydrodynamical form, Z. Phys. **40**, 322 (1927).
[40] B. Larder, D. O. Gericke, S. Richardson, P. Mabey, T. White, and G. Gregori, Fast nonadiabatic dynamics of many-body quantum systems, Sci. Adv. **5**, eaaw1634 (2019).
[41] A. P. Thompson, H. M. Aktulga, R. Berger, D. S. Bolintineanu, W. M. Brown, P. S. Crozier, P. J. In't Veld, A. Kohlmeyer, S. G. Moore, T. D. Nguyen *et al.*, Lammps-a flexible simulation tool for particle-based materials modeling at the atomic, meso, and continuum scales, Comput. Phys. Commun. **271**, 108171 (2022).
[42] P. Svensson, T. Campbell, F. Graziani, Z. Moldabekov, N. Lyu, V. S. Batista, S. Richardson, S. M. Vinko, and G. Gregori, Development of a new quantum trajectory molecular dynamics framework, Phil. Trans. R. Soc. A. **381**, 20220325 (2023).
[43] J. J. Monaghan, Smoothed particle hydrodynamics and its diverse applications, Annu. Rev. Fluid Mech. **44**, 323 (2012).
[44] V. Springel, Smoothed particle hydrodynamics in astrophysics, Annu. Rev. Astron. Astrophys. **48**, 391 (2010).
[45] D. J. Price, Smoothed particle hydrodynamics and magnetohydrodynamics, J. Comput. Phys. **231**, 759 (2012).
[46] R. A. Gingold and J. J. Monaghan, Smoothed particle hydrodynamics: Theory and application to non-spherical stars, Mon. Not. R. Astron. Soc. **181**, 375 (1977).
[47] B. Ben Moussa and J. P. Vila, Convergence of SPH method for scalar nonlinear conservation laws, SIAM J. Numer. Anal. **37**, 863 (2000).
[48] J. J. Monaghan, Smoothed particle hydrodynamics, Rep. Prog. Phys. **68**, 1703 (2005).
[49] F. Haas, A magnetohydrodynamic model for quantum plasmas, Phys. Plasmas **12**, 062117 (2005).
[50] R. Schmidt, B. J. B. Crowley, J. Mithen, and G. Gregori, Quantum hydrodynamics of strongly coupled electron fluids, Phys. Rev. E **85**, 046408 (2012).
[51] G. Manfredi, P.-A. Hervieux, and J. Hurst, Fluid descriptions of quantum plasmas, Reviews of Modern Plasma Physics **5**, 7 (2021).
[52] P. Mocz and S. Succi, Numerical solution of the nonlinear Schrödinger equation using smoothed-particle hydrodynamics, Phys. Rev. E **91**, 053304 (2015).
[53] G. Manfredi, How to model quantum plasmas, Fields Inst. Commun **46**, 263 (2005).
[54] M. Bonitz, Z. A. Moldabekov, and T. Ramazanov, Quantum hydrodynamics for plasmas–Quo vadis? Phys. Plasmas **26**, 090601 (2019).
[55] R. E. Wyatt, *Quantum Dynamics with Trajectories: Introduction to Quantum Hydrodynamics* (Springer Science & Business Media, Cham, 2005), Vol. 28.
[56] Z. Moldabekov, T. Dornheim, G. Gregori, F. Graziani, M. Bonitz, and A. Cangi, Towards a quantum fluid theory of correlated many-fermion systems from first principles, SciPost Phys. **12**, 062 (2022).
[57] G. Kelbg, Theorie des quanten-plasmas, Annalen der Physik **467**, 219 (1963).
[58] A. Filinov, M. Bonitz, and W. Ebeling, Improved Kelbg potential for correlated Coulomb systems, J. Phys. A: Math. Gen. **36**, 5957 (2003).
[59] D. J. Price and J. J. Monaghan, An energy-conserving formalism for adaptive gravitational force softening in smoothed particle hydrodynamics and *N*-body codes, Mon. Not. R. Astron. Soc. **374**, 1347 (2007).
[60] J. P. Morris, *Analysis of Smoothed Particle Hydrodynamics with Applications* (Monash University, Australia, 1996).
[61] J. J. Monaghan, Sph without a tensile instability, J. Comput. Phys. **159**, 290 (2000).
[62] J. M. Dawson, Particle simulation of plasmas, Rev. Mod. Phys. **55**, 403 (1983).
[63] M. D. Acciarri, C. Moore, L. P. Beving, and S. D. Baalrud, When should PIC simulations be applied to atmospheric pressure plasmas? impact of correlation heating, Plasma Sources Sci. Technol. **33**, 035009 (2024).
[64] L. Bai and D. Breen, Calculating center of mass in an unbounded 2D environment, J. Graph. Tools **13**, 53 (2008).
[65] M. Deserno and C. Holm, How to mesh up Ewald sums. I. A theoretical and numerical comparison of various particle mesh routines, J. Chem. Phys. **109**, 7678 (1998).
[66] D. J. Evans and B. L. Holian, The Nose–Hoover thermostat, J. Chem. Phys. **83**, 4069 (1985).
[67] R. Fatehi and M. T. Manzari, Error estimation in smoothed particle hydrodynamics and a new scheme for second derivatives, Comput. Math. Appl. **61**, 482 (2011).
[68] S. Korzilius, W. H. Schilders, and M. J. Anthonissen, An improved cspm approach for accurate second-derivative approximations with sph, J. Appl. Math. Phys. **05**, 168 (2017).

[69] M. Basa, N. J. Quinlan, and M. Lastiwka, Robustness and accuracy of SPH formulations for viscous flow, Int. J. Numer. Methods Fluids **60**, 1127 (2009).

[70] G. C. Ganzenmüller, M. O. Steinhauser, P. Van Liedekerke, and K. U. Leuven, The implementation of smooth particle hydrodynamics in LAMMPS, Paul Van Liedekerke Katholieke Universiteit Leuven **1**, 31 (2011).

[71] I. J. Schoenberg, Contributions to the problem of approximation of equidistant data by analytic functions. Part B. On the problem of osculatory interpolation: A second class of analytic approximation formulae, Q. Appl. Math. **4**, 112 (1946).

[72] J.-P. Hansen and I. R. McDonald, *Theory of Simple Liquids: With Applications to Soft Matter* (Academic Press, San Diego, CA, 2013).

[73] G. Gregori and D. O. Gericke, Low frequency structural dynamics of warm dense matter, Phys. Plasmas **16**, 056306 (2009).

[74] J. Wax and T. Bryk, An effective fitting scheme for the dynamic structure of pure liquids, J. Phys.: Condens. Matter **25**, 325104 (2013).

[75] M. Schörner, H. R. Rüter, M. French, and R. Redmer, Extending *ab initio* simulations for the ion-ion structure factor of warm dense aluminum to the hydrodynamic limit using neural network potentials, Phys. Rev. B **105**, 174310 (2022).

[76] G. Gregori, A. Ravasio, A. Höll, S. Glenzer, and S. Rose, Derivation of the static structure factor in strongly coupled non-equilibrium plasmas for x-ray scattering studies, High Energy Density Phys. **3**, 99 (2007).

[77] D. Pines, *Theory of Quantum Liquids: Normal Fermi Liquids* (CRC Press, Boca Raton, FL, 2018).

[78] J. Chihara, Difference in x-ray scattering between metallic and non-metallic liquids due to conduction electrons, J. Phys. F **17**, 295 (1987).

[79] J. Chihara, Interaction of photons with plasmas and liquid metals-photoabsorption and scattering, J. Phys.: Condens. Matter **12**, 231 (2000).

[80] P. Svensson, Y. Aziz, T. Dornheim, S. Azadi, P. Hollebon, A. Skelt, S. M. Vinko, and G. Gregori, Modeling of warm dense hydrogen via explicit real-time electron dynamics: Dynamic structure factors, Phys. Rev. E **110**, 055205 (2024).

[81] D. Pines and D. Bohm, A collective description of electron interactions: II. Collective vs individual particle aspects of the interactions, Phys. Rev. **85**, 338 (1952).

[82] T. Dornheim, S. Groth, J. Vorberger, and M. Bonitz, *Ab initio* path integral monte carlo results for the dynamic structure factor of correlated electrons: From the electron liquid to warm dense matter, Phys. Rev. Lett. **121**, 255001 (2018).

[83] C. Fortmann, A. Wierling, and G. Röpke, Influence of local-field corrections on thomson scattering in collision-dominated two-component plasmas, Phys. Rev. E **81**, 026405 (2010).